NASA CONTRACTOR REPORT

NASA CR-2267

N73- 25277
NASA CR-2267

CHARACTERISTICS OF DILUTE GAS-SOLIDS SUSPENSIONS IN DRAG REDUCING FLOW

by Ronald S. Kane and Robert Pfeffer

Prepared by
CITY UNIVERSITY OF NEW YORK
New York, N.Y. 10031
for Lewis Research Center

NATIONAL AERONAUTICS AND SPACE ADMINISTRATION • WASHINGTON, D. C. • JUNE 1973

1. Report No.
NASA CR-2267

2. Government Accession No.

3. Recipient's Catalog No.

4. Title and Subtitle
CHARACTERISTICS OF DILUTE GAS-SOLIDS SUSPENSIONS IN DRAG REDUCING FLOW

5. Report Date
June 1973

6. Performing Organization Code

7. Author(s)
Ronald S. Kane and Robert Pfeffer

8. Performing Organization Report No.
None

9. Performing Organization Name and Address
City University of New York
New York, New York 10031

10. Work Unit No.

11. Contract or Grant No.
NGL 33-013-029

12. Sponsoring Agency Name and Address
National Aeronautics and Space Administration
Washington, D.C. 20546

13. Type of Report and Period Covered
Contractor Report

14. Sponsoring Agency Code

15. Supplementary Notes
Project Manager, Henry A. Putre, Nuclear Systems Division, NASA Lewis Research Center, Cleveland, Ohio

16. Abstract

Measurements were performed on dilute flowing gas-solids suspensions and included data, with particles present, on gas friction factors, velocity profiles, turbulence intensity profiles, turbulent spectra, and particle velocity profiles. Glass beads of 10 to 60 micron diameter were suspended in air at Reynolds numbers of 10,000 to 25,000 and solids loading ratios from 0 to 4. Drag reduction was achieved for all particle sizes in vertical flow and for the smaller particle sizes in horizontal flow. The profile measurements in the vertical tube indicated that the presence of particles thickened the viscous sublayer. A quantitative theory based on particle-eddy interaction and viscous sublayer thickening has been proposed.

17. Key Words (Suggested by Author(s))
Dilute
Drag reduction
Pipe flow
Pressure drop
Suspension
Turbulence
Velocity profile
Viscous sublayer

18. Distribution Statement
Unclassified - unlimited

19. Security Classif. (of this report)
Unclassified

20. Security Classif. (of this page)
Unclassified

21. No. of Pages
91

22. Price*
$3.00

---

* For sale by the National Technical Information Service, Springfield, Virginia 22151

Table of Contents

Page

Tables

Figures

Page

Figures (cont.)

Summary

Flow measurements were performed on dilute gas-solids suspensions flowing in a closed loop system. The flow measurements included data, in the presence of particles, on gas friction factors, gas velocity profiles, gas turbulence intensity profiles, gas turbulent spectra, and particle velocity profiles. During flow measurements, glass beads ranging in size from 10 to 60 microns in average diameter by weight were suspended in air at gas Reynolds numbers of 10,000 to 25,000 and solids loading ratios from 0 to 4. Pressure drop measurements were taken in both horizontal and vertical 0.870 inch, inside diameter, stainless steel tubes. Profile measurements were taken only in the vertical tube.

Some novel and interesting techniques were used for measurement of various quantities in suspension flow such as solids loading ratio, gas velocity and turbulence profiles, and particle velocity profiles. A target-meter, with mounted strain gauges, was used in conjunction with a sharp-edged orifice to measure loading ratio during operation in the closed loop. A constant temperature anemometer with thermistor and fiber-film probes was used to measure gas properties in suspension flow. Particle velocities were measured by the double streak photographic method.

Drag reduction was achieved for all particle sizes in the vertical test section. The two largest particle sizes revealed drag increases in the horizontal test section. The results in the horizontal test section were complicated by gravity segregation and particle deposition. The profile measurements in the vertical section indicated that the presence of particles caused a thickening of the viscous sublayer and a general increase in turbulence intensity away from the sublayer region. The gas velocity profiles for suspension flow, in the turbulent core, were similar to

those without particles. The particle velocity profiles were similar, in the turbulent core, to the gas velocity profiles. A theory, based on particle-eddy interaction and viscous sublayer thickening has been proposed to explain these results.

Introduction

This report represents the first two phases of a three phase investigation (ref. 1) into the existence, causes, and effects of drag reduction. The first phase consisted of friction factor measurements to confirm the existence of the gaseous drag reduction that was reported in an earlier study (refs. 2-3). The second phase of the investigation consisted of gas velocity, gas turbulence intensity, gas turbulent spectra, and particle velocity profile measurements designed to elucidate the reasons for the drag reduction. The third phase consisted of heat transfer measurements to determine if Nusselt number reduction will occur with drag reduction. The heat transfer work has been reported separately. The results of the experimental investigation were intended to provide sufficient information to determine which of the suggested causes of drag reduction was the correct one. These suggested causes included reduction of gas viscosity (ref. 4), electrostatic effects (refs. 5-6), general turbulence suppression (ref. 7), and thickening of the viscous sublayer (refs. 8-10). The results were also intended to provide a basis for a quantitative theory predicting the amount of drag reduction.

Previous investigators have reported decreased gas friction factors when particles were added to a turbulent stream. A summary of earlier experimental evidence of drag reduction is shown in Table 1. Although experimental restrictions may have dictated the results, drag reduction has generally been limited to small particle sizes, small pipe diameters, low loading ratios, and low turbulent Reynolds numbers.

In this investigation, five different nominal sizes of glass beads (designated by the manufacturer as #980, #981, #279, #380, and #660) ranging from 10 microns to 60 microns in diameter were suspended in air at gas Reynolds numbers of 10,000 to 25,000 and solids loading ratios from 0 to 4. The frictional pressure drop of air in two 0.870 inch, inside diameter, stainless steel test sections, one vertical and one horizontal, was measured for both clean gas and suspension flow. A reduction of the air friction factor in suspension flow below that of the friction factor in clean gas flow at the same gas Reynolds number was defined as drag reduction. Because gravity segregation could be discounted in the vertical test section, all profile measurements were restricted to the vertical test section.

One of the difficulties attending experimental investigation of gas-solids suspensions has been the general unsuitability of many instruments that otherwise perform adequately in clean gas service (ref. 11). As a byproduct of this investigation, some novel and interesting measurement techniques were developed and refined. These techniques included use of a target-meter and orifice to measure the solids loading ratio in a closed loop system, a fiber-film probe and a constant temperature anemometer to measure gas mean velocity, gas turbulent intensity and spectral profiles, in suspension flow, and a high speed strobe and camera to measure particle velocity profiles.

Experimental Apparatus and Procedures

The suspension was circulated through the closed loop system shown in Figure 1. The loop could have been described as a 12 foot high, 18½ foot long rectangle generally constructed of 1 inch, outside diameter, 0.065 inch wall, type 304 stainless steel tubing. The motive force for flow was provided by a centrifugal circulator which was capable of pumping gas and solids simultaneously.

Two test sections for pressure drop measurements were provided. The vertical test section was 30 inches long and fabricated, like the 92 tube diameter entrance region, from 1 inch outside diameter, 0.065 inch wall, type 304 stainless steel tubing. The pressure taps, at either end of the 30 inch test section, were fabricated from 1/16 inch outside diameter, 0.020 inch inside diameter, stainless steel tubing and seated to match 0.020 inch holes in the wall of the test section. After soldering the taps to the test section, the tap holes were lightly polished to eliminate burrs. The horizontal test section was identical to the vertical test section but had a 173 tube diameter entrance region. The taps were located at the top of the horizontal test section to avoid plugging by particle deposition.

Two 1 inch, inside diameter, pyrex viewing sections, one in the vertical downflow section and one in the lower horizontal section were installed in the loop using glass-to-steel flanges. In order to prevent accumulation of static electric charges, a continuous leakage path to a common ground was maintained by attaching cables across the pyrex sections.

A mass flowmeter, containing a sharp-edged orifice and a cantilevered target as integral units, was located in the downward vertical section of the loop. A cross section of the mass flowmeter is shown in Figure 2. The orifice was used to measure the gas flow rate even with particles in suspension. Earlier studies (refs. 1-3) and this one showed that the calibration of an orifice was unaffected by dilute volumetric concentrations of solids suspended in the gas. The target was used, in conjunction with strain gauges mounted on the target support, to measure the total flow rate. With the gas flow rate known from the orifice, the solids flow rate was determined. (The calibration of this device is given in a later section.)

The gas profile measurements were taken just above the vertical pressure drop test section. An electronic anemometer unit consisting of a constant temperature anemometer, an auxiliary filter and gain control, a D.C. voltmeter, and an r.m.s. voltmeter was used. Four different types of anemometer probes were tested or used: thermistor, conical wedge film, hot wire, and fiber-film.

The thermistor probe was used only for some preliminary calibration work because its large size (making it strong enough to withstand the bombardment of particles) destroyed the sensitivity of the probe to most of the turbulence. The probe was also difficult to use because it was extremely sensitive to small ambient temperature changes. The conical wedge film was also too large for meaningful measurements. The hot wire, although having the most sensitivity to turbulence, was unsuitable for suspension measurements because it could not withstand the bombardment of particles.

The fiber-film probe was chosen for measurements in suspension flow. The probe was only slightly temperature sensitive and registered about 60 to 70 percent of the turbulence registered by the hot wire. The probe failed after several hours use in a dilute suspension of 30 micron particles because of the loss of the protective quartz coating over the film sensor. However, the probe life was sufficient to obtain measurements of flow and turbulence quantities over a wide variety of flow conditions.

The probes were positioned at various radial locations in the tube using a gear operated traverse mechanism. The probes were calibrated outside of the loop using a commercial calibration wind tunnel. The complete details of the calibrations and calibration procedures are available in reference 1.

For photographic measurement of particle velocity profiles, the vertical stainless steel test section was replaced with a section of 1 inch, inside diameter, clear pyrex pipe. The camera, a 35 mm single lens reflex with a 32 mm macrolens on a bellows extension, was set to record two spaced shadow streaks of the particles on the same frame. The film was exposed twice by a high speed strobe during a short, known time interval. The measured distance between two shadow streaks on a photograph represented the movement of a particle over a known time interval and therefore determined the particle velocity.

Solids were added to the loop before data runs by pouring a given weight of sifted particles into the solids inlet port located near the circulator intake. The port was sealed and the circulator was started to disperse the particles through the loop With the exception of mass flowmeter calibrations, the system was always operated in a closed loop condition.

Calibrations and Clean Gas Test Results

Particle Size Analyses

The five grades of glass beads were sized before and after circulation in order to define the size limits of the solids and to determine the extent of particle degradation caused by prolonged circulation in a closed loop system. A Coulter Counter was used for the particle size analyses. The results are given in Table 2 where weight mean and arithmetic mean diameters are given.

Before circulation, all the glass beads, with the exception of the #660 designation, had narrow distributions and the two mean diameters were similar. After circulation, the particle degradation tended to slightly broaden the distributions. Nevertheless, the diameters did not change significantly except for the #660 beads which suffered a three-fold reduction in size.

Target-meter Calibration

The target-meter was calibrated in an open loop operation whereby a known weight of particles was collected in a known time interval, providing a direct measure of the solids flow rate. The flow of solids and gas together affected the deflection of the strain gauge mounted target-meter. Therefore, the two effects needed to be separated for calibration.

The calibration of the meter was based on the fact that the deflection of the cantilevered target support was directly proportional to the force of the fluid impinging on the target. The force of the gas alone was known from the flow rate given by the sharp-edged orifice. The force of the solids was related to the solids flow rate.

Because the electronic processing and recording system did not impose any non-linear gain on the strain gauge signal, it was expected and confirmed that the recorder output was linear with the force acting on the target. This result is shown on Figure 3 where recorder output voltage is plotted against the air drag force on the target. The open loop calibrations indicated that the force of the solids striking the target also gave a linear readout. However, the calibration of the device against solids drag force showed that the calibration was a strong function of the particle diameter. Therefore, separate calibrations were developed for the different particle sizes. The variation in the calibrations was attributed to the different velocities at which different particle sizes struck the target - smaller particles struck the target at higher velocities than the larger ones for the same air velocity.

In general:

$$V_{ST} \propto F = F_g + F_p \tag{1}$$

For clean gas flow (ref. 1):

$$V_{STO} = 45.6F_g + 0.011 \tag{2}$$

$$= 45.6C_D A_T \frac{\rho U^2}{2g_c} + 0.011$$

where C_D and A_T are constants. The open loop calibrations gave (ref. 1):

$$F_p \propto V_{ST} - V_{STO} = 95.2 \frac{A_T}{A_p} \frac{W_p U}{g_c} \tag{3}$$

$$F_p \propto V_{ST} - V_{STO} = 40.4 \frac{A_T}{A_p} \frac{W_p U}{g_c} \tag{4}$$

$$F_p \propto V_{ST} - V_{STO} \doteq 24.8 \frac{A_T}{A_p} \frac{W_p U}{g_c} \tag{5}$$

for the #279, #380, and #660 glass beads respectively. Equations 1 through 5 were combined to give formulae for the loading ratio:

$$\eta = \frac{W_p}{\rho U A_p} = \frac{248}{\rho U^2} [V_{ST} - 0.011] - 0.264 \tag{6}$$

$$\eta = \frac{W_p}{\rho U A_p} = \frac{583}{\rho U^2} [V_{ST} - 0.011] - 0.620 \qquad (7)$$

$$\eta = \frac{W_p}{\rho U A_p} = \frac{952}{\rho U^2} [V_{ST} - 0.011] - 1.011 \qquad (8)$$

for the #279, #380, and #660 glass beads respectively.

Open loop calibrations were not performed for the #980 and #981 glass beads because the large and expensive inventory of these beads required for the calibrations was not available. However, the #981 glass beads were almost exactly the same size as the #279 glass beads and a separate calibration was obviously not required. Because it seemed that the #279 glass beads, even in the disturbed region upstream of the target, had accelerated to the air velocity (ref. 1), the smaller #980 glass beads were assumed to also have nearly the same velocity as the air as they struck the target. Therefore, the calibration for the #279 glass beads was also used for the #980 glass beads. Again, complete details of the calibration procedure and results can be found in reference 1.

Clean Air Friction Factors

The clean air pressure drop measurements showed no discernible difference between the results obtained in the vertical test section and those obtained in the horizontal test section. The Blasius equation for friction factor:

$$f_g = \frac{0.316}{Re_g^{\,0.250}} \qquad (9)$$

which is considered accurate (ref. 12) to ±5% could have been used to correlate the data within 3%. However, the empirical equation:

$$f_g = \frac{0.524}{Re_g^{0.302}} \tag{10}$$

was used to correlate the data to ±1%. In the working range of Reynolds numbers used in the study, the empirical equation predicts slightly higher friction factors than does the Blasius equation. However, this was perfectly consistent with the standard Moody diagram (ref. 12) and the small but finite roughness associated with commercially drawn tubing.

Clean Air Velocity Profiles

The clean air velocity profiles were correlated by the single power law profile:

$$\frac{U}{U_c} = \left(\frac{y}{R}\right)^{1/6.62} \tag{11}$$

for Reynolds numbers between 12,000 and 22,000. Schlichting (ref. 13) reports that the exponent has the value 1/6.60 at a Reynolds number of 23,000. The measured profiles were therefore only slightly flatter than expected, the additional flatness perhaps the result of the disturbances produced by the anemometer inlet port and the probe support.

In terms of the friction velocity and the universal velocity profile, the profiles were correlated by the logarithmic law (ref. 13) in the turbulent core region:

$$\frac{U}{U_*} = 2.5\ell n \frac{yU_*}{\nu} + 5.5 \tag{12}$$

The slight deviation of the data below this law at the edge of the buffer layer and above the law at high values of yU_*/ν was in agreement with the results of other studies (ref. 14). Because of the small tube size, the velocity profiles carried only into the outside edge of the buffer layer and not at all into the viscous sublayer.

Clean Air Turbulence Intensities

The measurement of clean air turbulence profiles revealed that the actual numerical results, although not necessarily the trends, were strongly dependent on the type of probe and the operating procedure. In this study, the clean air turbulence intensities measured with the fiber-film probes were used for comparison with the suspension results. The clean air turbulence intensity profiles are shown in Figure 4.

The trends reported in Figure 4 are in agreement with results of other investigators (refs. 15-16). The turbulence intensity relative to the local mean velocity increased from the tube centerline, slowly at first, and then rapidly as the wall was approached. The turbulence intensity relative to the local mean velocity at a fixed radial position decreased with increased values of Reynolds number. Because measurements were not taken deep in the buffer layer or in the viscous sublayer, the known sharp maximum at the edge of the sublayer and the decrease of the turbulence intensity to zero at the wall (ref. 15) were not observed.

The spectral profiles indicated that the fiber-film probe was quite limited in sensitivity to high wave numbers (small eddies) and could not give the response of a smaller probe like a hot-wire. Unfortunately, the hot-wire was not suitable for suspension measurements. Therefore, meaningful information on the effect of particles on various eddy sizes could not be obtained. Fortunately this difficulty did not extend to measurements of the effect of particles on the overall turbulence level at a particular location. Further discussion of this point is given in reference 1.

Suspension Test Results and Discussion

The results of the experimental program confirmed the existence of drag reduction in a gas-solids suspension. This section includes detailed description of the experimental results obtained with suspension flow and comparison, where applicable, to the results of other investigations. The section begins with some comments and observations on the behavior of the suspended particles in the closed loop. The rest of the section describes the results of the pressure drop and profile measurements in suspension flow.

Observations on Flow and Solids Entrainment

Graphs of loading ratio versus weight added to the loop were developed for all particle sizes and gas Reynolds number ranges. Two of these are shown in Figures 5 and 6 for the #980 and #380 glass beads, respectively. The graphs were plotted from data accumulated during selected runs following thorough loop cleanings but at varied ambient conditions. It was apparent from these graphs and additional data (not shown) that the exact value of the loading ratio corresponding to a particular weight of solids added depended on a multitude of factors. The most important of these factors were the particle size, gas Reynolds number, ambient humidity, and the amount of particles remaining in dead spots after a loop cleanout. The effect of the first two factors can be seen qualitatively from the figures. The effect of the last two was even more qualitative and could not be seen from the figures.

Large particles permitted circulation of higher loading ratios than smaller particle sizes. For example, adding 100 grams of #380 glass beads to a clean loop resulted in an average loading ratio of about 1.0 whereas adding the same amount of #980 glass beads to a clean loop resulted in a loading ratio of about 0.1, a full order of magnitude difference. The larger Reynolds numbers also permitted circulation at higher loading ratios, although the Reynolds number effect was not as important or as consistent as the particle size effect. The proportionate spread of loading ratio at a particular value of weight added was roughly equal to the proportionate spread in gas Reynolds numbers.

The shapes of the loading ratio curves were similar for the #981, #279, and #380 glass beads. For each of these three particle designations, the first 40 grams added produced little entrainment. The next 60 grams added produced significant entrainment. Additional weight added over 100 grams did not consistently increase entrainment except at the highest Reynolds numbers. Unfortunately, the circulator could not sustain the highest Reynolds numbers with large quantities of solids in the loop because of excessive power requirements. Therefore, adding more than 140 grams often did not increase the loading ratio and occasionally decreased the loading ratio with the appearance of saltation in the horizontal sections.

The shape of the loading ratio curve for the #660 glass beads differed from the ones discussed above only at low loading ratios. The first 40 grams of weight added did produce significant entrainment although the same tendency of the curves to level off at high values of weight added appeared. A certain amount of caution must be introduced in evaluating the results for the #660 beads because of the unknown effect of the attrition of the #660 beads on the target-meter response. The Brush recorder reading did not appear to change with time as the #660 glass bead suspension circulated and as the particles attrited. An increasing proportion of fine particles would have been expected to increase the reading with time. Alternatively an increasing proportion of fine particles would have contributed to a loss of entrainment by particle deposition. The two effects apparently offset each other in terms of the recorder reading. However, there is no way of assessing the effect of the particle attrition upon the target-meter calibration. The open loop calibration did not account for attrition since particles passed only once through the circulator before collection and did not have time to undergo significant diameter changes.

The loading ratio curve for the #980 glass beads was much flatter than for the other particles indicating the great difficulty encountered in circulating fine particles. The difficulty was attributed to the importance of electrostatic charging and cohesion upon the behavior of small particles. Both conditions are more important in suspensions of small particles than large ones because both conditions are aided by increased contact and surface area. The #980 beads in suspension gave obvious evidence of electrostatic deposition in the form of herringbone patterns on the walls of the pyrex viewing sections. Further addition of particles at first removed the deposits but then they reformed and became almost impossible to remove. Similar phenomena have been observed by Boothroyd (ref. 11), Wachtell and Waggener (ref. 17), and Rossetti (ref. 2). The cohesiveness of the various particle sizes was obvious from preliminary screening of the particles before addition to the loop. The #660 and #380 glass beads poured through the screen while the #279 and #981 glass beads required some mechanical aid to pass through. However, the #980 glass beads, particularly when the laboratory humidity was higher than normal, almost had to be forced through the same screen.

All of the particle sizes were subject to some form of deposition at isolated locations in the loop. The one common property of all the deposit locations was that they represented a discontinuity of some physical loop characteristics. The first type of discontinuity was the least serious: the locations where the stainless steel charge leakage path was interrupted by the nonconducting pyrex viewing sections. Only the #980 glass beads formed uniform deposits on the pyrex viewing sections.

Other particle designations deposited on the lower wall of the horizontal pyrex viewing section. However, this type of deposit could be considered as occurring at a second type of discontinuity: the locations where the flow expanded in cross sectional area producing a sudden decrease in velocity. Two mechanisms contributed to deposition at flow expansions and disturbances. In horizontal sections, large agglomerates of small particles fell out of suspension as the flow velocity decreased. In vertical sections, smaller particles tended to follow eddy patterns caused by flow disturbances and deposit in dead spots. This phenomenon was most apparent at the target-meter location where heavy deposits, as much as 40 grams, of small particles were often found filling the tube containing the target-meter support. Large individual particles were less prone to leave the main flow pattern. The third type of discontinuity, a thermal one, was caused by the water cooling jacket located just upstream of the circulator. Thermophoresis apparently caused the finer particles to plate out on the cool wall of the jacketed tubing.

The ability of a particle to deposit at any of the three types of discontinuities increased with decreasing particle size. The loading ratio curves reflected this ability. Partially because the amount of deposition could not be controlled, the loading ratio curves did not provide information to accurately predict the amount of entrainment. Only the target-meter response gave reliable indications of the loading ratio for a given run.

The two other factors that were not incorporated into the loading ratio curves also prevented use of the curves as calibrations. The laboratory relative humidity while usually less than 50%, was not regulated but appeared to have a marked effect on the cohesiveness of the particles. The amount of particles remaining in dead spots after a loop cleanout was also not controlled. When runs with a designated particle size were in progress, the loop cleanout procedure did not include removal of particles that had accumulated in dead spots such as the three-way ball valve body cavity, the tube holding the target-meter, and the circulator shaft bearings. Only when particle sizes were changed or when clean air data was required was every trace of particle accumulation removed with a high pressure airhose and an industrial vacuum cleaner. In general, less than thorough cleanings permitted higher loading ratios.

After prolonged circulation in the closed loop, it was possible to differentiate the various glass bead particle designations by their color. The glass beads before circulation were white. After circulation their color ranged from an off-white to a dark gray with increasing darkness corresponding to their nominal size before circulation. The color of the #660 glass beads suggested that bits of stainless steel were mixed with the bead sample. The likely source of the eroded stainless steel was the pump impeller and impeller housing.

Suspension Friction Factors

Unlike the clean air pressure drop measurements, suspension pressure drop measurements involved a correction for static head in the vertical test section in order to determine the frictional pressure drop. In the general case the pressure drop across a test section containing a gas-solids suspension is:

$$\Delta P = \Delta P_{ag} + \Delta P_{ads} + \Delta P_{Lg} + \Delta P_{Lds} + \Delta P_{fg} + \Delta P_{fds} \qquad (13)$$

The pressure drop caused by acceleration of gas was negligible because the flow was fully developed and isothermal in both test sections. The pressure drop caused by acceleration of the solids was also negligible because the bulk slip velocity, as reported in a later section of this report, was small and the solids acceleration pressure drop could be related directly to the gas acceleration pressure drop (ref. 11).

$$\Delta P_{ads} \cong \frac{W_p}{W_g} \Delta P_{ag} \qquad (14)$$

The static head of air was automatically balanced by the physical configuration of the micromanometer. However, the static head of solids in the vertical test section had to be subtracted from the reading of the micromanometer in order to determine the frictional pressure drop. The loading ratio was assumed to be the same as the ratio of the dispersed solids density to the air density. Therefore:

$$\Delta P_{Lds} = \rho_{ds} \frac{gL}{g_c} = \eta\rho \frac{gL}{g_c} \qquad (15)$$

was assumed. This would be true only if the bulk slip velocity between the gas and solids was negligible which was verified later by the particle velocity profile measurements.

The pressure drop caused by fluid friction and by solids friction could not be differentiated by the micromanometer so that both were combined into one frictional term:

$$\Delta P_f = \Delta P_{fg} + \Delta P_{fds} \tag{16}$$

The frictional pressure drops were used to calculate friction factors from the equation:

$$f_s = \frac{2\Delta P_f g_c D}{\rho U^2 L} \tag{17}$$

The air density was used in the friction factor calculations in order to provide a direct comparison between clean air and suspension friction factors.

The results of the pressure drop measurements are shown in Figure 7 for the #980, #981, and #279 glass beads in the vertical test section and in Figures 8 and 9 for the #380 and #660 glass beads, respectively in the vertical test section. The graphs were plotted as the ratio of the suspension friction factor to the clean gas friction factor versus loading ratio at corresponding gas Reynolds numbers. Drag reduction was indicated by values of the friction factor ratio below unity.

Drag reduction was achieved for all five glass bead designations in the vertical test section. The maximum drag reduction was about 40% for both the #380 and #660 glass beads. The onset of drag reduction with loading ratio was progressively delayed with increasing particle size. For the #380 and #660 glass beads, which showed a variation of drag reduction with gas Reynolds number, the onset of drag reduction was also delayed with increasing gas Reynolds number. Only the friction factor ratio curve for the #380 glass beads at a gas Reynolds number of about 18,000, showed a distinct minimum. All other curves, after the onset of drag reduction, either showed a monotonic decrease of friction factor ratio or a decrease to a uniform level of drag reduction. In general, the friction factor ratio remained near unity until the onset of drag reduction. However, the #660 glass beads showed a sizable drag increase before the onset of drag reduction. As already mentioned when the loading ratio curve for this particle size was discussed, some caution must be introduced into any conclusions drawn from the results obtained with the #660 beads because of significant particle attrition.

The results for the #980, #981, and #279 glass beads were very similar although the maximum amount of drag reduction for the #980 glass beads was slightly smaller at 10% compared to 13% achieved for the #981 and #279 glass beads. As expected, the results for the #981 and #279 glass beads were almost identical. The onset of drag reduction appeared at a slightly lower loading ratio (0.10) for the #980 glass beads than for the #981 and #279 glass beads (0.15). The friction factor ratio curves for these particle designations showed a decrease to a moderate uniform level of drag reduction but no distinct minimum. The slight drag increase, 2%, at very low loading ratios for the #981 and #279 glass beads was probably caused by a combination of solids friction and additional tube roughness produced by a small amount of particle deposition.

The flow of suspensions of #380 glass beads produced drag reductions of as much as 36%. The onset of drag reduction was delayed until loading ratios of 0.2 to 1.0 depending on the gas Reynolds number. After the onset of drag reduction, decrease in friction factor ratio was monotonic at all Reynolds numbers except at a Reynolds number of about 18,000 where a distinct minimum at a loading ratio of 2.0 was achieved. At this Reynolds number and for this particle designation, the pump was able to circulate high loading ratios without significant loss of entrainment. A distinct minimum would probably have been achieved for all the other curves and particle designations if high enough loading ratios could have been attained. Before the onset of drag reduction, the friction factor ratio remained at or slightly above unity.

For the #660 glass beads, drag reduction of as much as 39% was achieved. The onset of drag reduction was further delayed until loading ratios of 1.0 to 1.8 depending on the gas Reynolds numbers. After the onset of drag reduction, the decrease in friction factor ratio was generally monotonic. The data for Reynolds numbers of about 18,000 suggested that a minimum similar to that of the #380 glass beads had been achieved. However, an insufficient number of experimental points could be obtained at these high loading ratios to conclusively define the minimum location. Again the results for this particle designation are clouded by the unknown effects of particle attrition.

The results of the pressure drop measurements are shown in Figure 10 for the #980, #981, and #279 glass beads in the horizontal test section and in Figure 11 for the #380 and #660 glass beads, respectively, in the horizontal test section. The results were almost identical to the results obtained in the vertical test section for the three smallest glass bead sizes. The #380 and #660 glass bead suspensions yielded drag increases rather than drag reduction in the horizontal test section. Apparently gravity segregation and sedimentation had a negligible effect upon the drag reducing ability of the smaller particle sizes but had a detrimental effect upon that of the larger particle sizes. The maximum drag increase for the #380 glass beads was 21%; for the #660 glass beads it was 44%. No Reynolds number effect was discernible for any of the five glass bead designations. The difference in results for the two test sections indicated that uniform particle distribution was important for the existence of drag reduction.

While several earlier investigations have measured drag reduction in gas-solids suspensions, only one reported data for the range of Reynolds numbers and particle sizes considered in this study. Rossetti (ref. 2), using the identical mass flowmeter and circulator and a similar closed loop system also measured drag reduction in vertical and horizontal test sections at Reynolds numbers between 10,000 and 25,000 and particle sizes between 10 and 60μ. The particles used were also the same glass bead designations, #980, #981, #279, #380, and #660.

The trends of the Rossetti results were almost identical to the ones reported here. Drag reduction was achieved for suspensions of all five particle designations in the vertical test section and for suspensions of all but the #380 and #660 glass beads in the horizontal section. The maximum drag reduction was achieved for the #380 and #660 glass beads in the vertical test section. The #980, #981, and #279 glass bead suspensions gave similar results in both the vertical and horizontal test sections. Drag increases were noted for the #380 and #660 glass beads in the horizontal test section.

There was a significant difference in the numerical results of the Rossetti study and the results of this study, especially in the vertical test section, because Rossetti did not establish separate target-meter calibrations for the different particle sizes and applied his loading-ratio calibration for the #380 glass beads to all glass bead designations. The loading ratio appeared in the calculation of the frictional pressure drop in the vertical test section and strongly affected the amount of drag reduction. A further cause of difference between the Rossetti results and the ones reported here was the difference in the size and material of construction of the two vertical test sections. Rossetti worked with a 1 inch inside diameter pyrex pipe following a 0.870 inch inside diameter stainless steel entrance region. The vertical test section here was a 0.870 inch inside diameter stainless steel tube preceded by a long length of identical 0.870 inch inside diameter stainless steel tubing. Numerical comparison of the vertical test section results is obviously inappropriate. However, the two studies did indicate that test section electrical characteristics have no effect on the existence of gas-solids drag reduction.

The horizontal test sections were fabricated from identical material in the two studies; and, numerical comparison between the two studies is possible in a limited context. It must be assumed for the purposes of comparison that the maximum loading ratios achieved by Rossetti were somewhat higher than the ones achieved here because Rossetti was able to attain higher Reynolds numbers. The loop used by Rossetti was shorter than this one and had a lower total frictional resistance to flow. It could, therefore, sustain higher air flow rates and better solids entrainment.

The maximum amount of drag reduction reported by Rossetti in the horizontal test section for the #980, #981, and #279 glass beads only slightly exceeded the amount reported in this study. The maximum amount of drag increase, reported by Rossetti, in the horizontal test section for the #380 and #660 glass beads almost exactly corresponded to the amount reported in this study. The shape of the friction factor ratio curves for the #380 glass beads were very similar for both studies.

Rossetti did not report distinct minima: however, three other investigators have reported the appearance of distinct minima at loading ratios between 1.0 and 2.0. The three investigations (ref. 7, 18, and 19) were conducted at a variety of Reynolds numbers, tube sizes, and particle diameters and could not be used for direct numerical comparison with the results of this study. The amount of reported maximum drag reduction varied from 5% (ref. 7) to 70% (ref. 18). However, there appeared to be uniform agreement that an optimum loading ratio existed for drag reduction. The fact that the optimum occurred in a dilute suspension emphasized the danger of extrapolating results of dense phase tests to describe the behavior of dilute suspensions. The wide variety of experimental apparatus and material used in other investigations and the painstaking care taken in this investigation to eliminate experimental assumptions proved conclusively that gas-solids drag reduction is a real phenomenon and is not a result of questionable data reduction and experimental techniques.

Suspension Air Velocity Profiles

Thirty air velocity profiles were measured for a wide variety of suspension conditions. All thirty profiles were similar to the corresponding clean air velocity profiles. Figure 12 shows the results of the two profiles taken near the maximum drag reducing conditions for the #380 and #279 glass beads. The suspension data have been superimposed on the curve fitting the clean air velocity profile data. The small difference between the suspension data points and the clean air curve was within the limits of scatter of the clean air velocity profile data.

Three investigations have been reported in the literature which include measurement of the air velocity profiles in the presence of dilute loadings (loading ratios less than 2.5) of small (less than 100μ diameter) particles. They all reported (ref. 8, 20, and 21) that air velocity profiles were essentially unchanged from clean air profiles. The earlier measurements were taken with pitot tubes. This study provided the first confirmation of the previous results using a different measurement technique, fiber-film anemometry.

Figure 13 shows the two profiles for the #380 and #279 glass beads replotted in terms of the friction velocity and the universal velocity profile. The curve fitting the clean air data has been shown for comparison. The universal suspension profiles for drag reducing conditions fell above the profiles for the clean air conditions. The general shape of the profiles were the same for all cases. However, the deviation of the profiles below a logarithmic law began sooner for the suspension profiles than for the clean gas profiles. The implication drawn from the results was that the viscous sublayer and buffer layer profiles extended further from the wall in the drag reducing suspension than in the clean gas. In other words, the viscous sublayer and the buffer layer had thickened.

Both Soo (ref. 7) and Peskin and Dwyer (ref. 8) suggested that the large spacing of the particles in a dilute suspension would permit the fluid to retain its original profile. However, both also suggested that the particles could introduce additional viscous dissipation into the fluid. Peskin and Dwyer further stated that particles occupying only a small volume could produce a thickened viscous sublayer and decrease the shear stress at the wall.

This investigation was the first reporting a thickened viscous sublayer in a gas-solids suspension. However, other investigators working with different media have reported the same phenomena. Eissenberg and Bogue (ref. 9) reported a thickened sublayer for aqueous drag reducing suspensions of flocculated thoria. Rudd (ref. 22) reported a thickened sublayer for drag reducing solutions of 0.01% Separan in water. The similarity of the results for the two early investigations and this one strongly indicate that drag reduction is the result of an interaction between the additive and the turbulent fluid in the near wall region.

Suspension Air Turbulence Intensities

Turbulence intensity profiles were measured simultaneously with the suspension air velocity profiles using the fiber-film probe. The profiles all indicated that the presence of particles had the effect of increasing the air turbulence above clean air values.

Figures 14 and 15 show the results of two relative turbulence intensity profiles taken near the maximum drag reducing conditions for the #380 and #279 glass beads. Both profiles revealed higher turbulence intensities at all traverse locations compared to the clean air values. The increase was small until the wall was approached where the increase was dramatic. For example, the percent relative turbulence intensity at the traverse location nearest the wall was 7.5% for clean air at a Reynolds number of about 18,000. The percent relative turbulence at this location for the suspensions of Figures 14 and 15 was 10.2% and 9.75%, respectively.

The result was in direct conflict with theories of drag reduction which predict an overall suppression of turbulence by the particles. Because of the conflict, the measurements were repeated for both clean air and suspension flows several times with the same results. The possible increase in measured turbulence caused by probe vibration was found to be negligible from the results of measurements made with a probe isolated from the flow but subject to the mechanical vibrations of the pump.

Only one other investigator (ref. 2) has directly measured turbulence intensities in a gas-solids suspension using anemometry. Rossetti used a thermister probe to record turbulence intensities at the centerline of a vertical section of his closed loop system. His measurements indicated that the turbulence intensities increased with loading ratio and drag reducing ability of the suspended solids. The results of this study were in general agreement with the results of the Rossetti work. Boothroyd (ref. 23) attempted to measure eddy diffusivity in vertical flowing and drag reducing gas-solids suspensions using gas dispersion techniques, and was unable to obtain consistent results. Peskin performed two studies on a non-drag-reducing suspension in a horizontal square duct and found in both cases that turbulence intensities decreased. The first study (ref. 24) used a helium gas tracer technique and the second study (ref. 25) used a glow discharge probe. However, it has been reliably confirmed by several investigators using hot-film anemometry (ref. 26) and laser Dopplermetry that the effect of adding small quantities of drag reducing polymers to water is to increase the turbulence intensities.

Figure 16 shows the results of Figure 14 normalized with friction velocity and plotted against nondimensional distance to the wall. The envelope of the clean air data has been included for comparison. Figure 14 enforced the conclusion that drag reduction in a gas-solids suspension could be characterized by a thickening of the viscous sublayer. The known sharp increase in turbulence intensities in the buffer layer and outer edge of the viscous sublayer had been shifted away from the wall. Rudd, for one, also reported the same outward shift in the peak values of turbulence intensities. Therefore, it can be concluded, as pointed out by Davies (ref. 27) that there is no general turbulence suppression in a drag reducing fluid.

Particle Velocity Profiles

Particle velocity profiles were measured for the three largest glass bead sizes. Two profiles at different loading ratios were taken at approximately the same gas Reynolds numbers for the #660 glass beads. One profile each was taken for the #380 and #279 glass beads. Although the double flash photographic streak patterns for the #660 glass beads were easily recognized, the patterns became difficult to discern with the smaller particle sizes. Because the streaks caused by the movement of the #279 particles were barely visible, velocity profiles for the smaller #980 glass beads were not measured.

The results shown in Figure 17 for the specific case of the #660 beads at a loading ratio of 2.23 and a gas Reynolds number of 16,400 were nevertheless, typical of all particle velocity profiles, regardless of particle size, loading ratio, or gas Reynolds number. The particle velocity profiles were, within the limits of the camera resolution and measurement accuracy, the same as the air velocity profiles with the exception of a finite slip velocity at the wall. (The last point of the photographic traverse was measured at the wall and always indicated a finite velocity.) The smaller #980 glass beads would certainly have shown the same tendency toward following the mean value of the local gas velocity. The finite depth of field of the camera prevented utilization of the photographs to determine accurate values of the slip velocity in the viscous sublayer. However, the results confirmed the assumption that the loading ratio could be used to approximate the ratio of the dispersed solids density to the air density in the vertical test section.

The results were not unexpected because the terminal settling velocities of the beads were only 0.744, 0.329, and 0.119 feet per second for the #660, #380, and #279 glass beads, respectively. Apparently, the particle separation in the vertical test section, even at the highest loading ratios of the study, was large enough to minimize the number of collisions among particles and to minimize the slip velocity between the gas and the particles. Although there is some question of the applicability of a continuum theory to the widely dispersed particles of a dilute suspension (refs. 7 and 11) the theory of Soo and Tung (ref. 28) also suggests that the particle velocity profile should approach that of the gas for particles with small relaxation times and negligible electrical charge.

The literature on direct photographic measurement of particle velocities in the turbulent flow of a gas-solids suspension in a vertical tube includes the work of Doig and Roper (ref. 29), Reddy, Van Wijk, and Pei (ref. 30), Reddy and Pei (ref. 31), and Kramer and Depew (ref. 21). The results reported by Doig and Roper do not provide a good comparison to this study because the particle diameters, 304μ and 756μ, were much larger than the ones considered here.

Reddy and Pei considered 100, 150, 200, and 250μ glass beads in suspension at loading ratios of 0.02, 0.06, 0.10, 0.15, 0.20, 0.40, and 0.60 and gas Reynolds numbers of 55,000; 78,000; and 100,000. They reported that the particle axial velocity profile in the turbulent core was similar to that of the gas and could be described by a power law relationship. The equation:

$$\frac{V_{pcs}}{V_t} = 1.0 + 1.59\eta^{2/3} \qquad (18)$$

was proposed to account for the variation of the centerline slip velocity with particle diameter and loading ratio. If this equation is extrapolated to the experimental range of this investigation, the centerline slip velocity (defined as the difference between the gas velocity and the particle velocity) corresponding to the conditions of Figure 17 is only 2.76 feet per second, well within the limits of experimental uncertainty. Therefore, this study was in substantial agreement with the results of Reddy and Pei.

Kramer and Depew reported the velocity profiles of 62μ and 200μ spherical glass beads in 0.5, 0.75, and 1.0 inch diameter tubes containing suspensions at gas Reynolds numbers from 5,760 to 50,000 and loading ratios from 0 to 5.0. The range of parameters for the 62μ glass beads corresponded closely to the range of parameters investigated during this study for the #660 glass beads. Kramer and Depew found that the slip velocity was quite small for the 62μ glass beads and did not vary significantly with loading ratio. The slip velocity did vary with the radial coordinate and decreased, even to negative values, toward the wall. The results of this study were in good agreement with those of Kramer and Depew. Therefore, this study confirmed the contention of Kramer and Depew that their continuum approach (ref. 32)to the calculation of suspension velocity profiles which predicted significant bulk slip velocities requires modification to provide better agreement of calculated results with experimental results for small particle sizes.

Theoretical Development and Discussion

The results of the profile measurements lent strong support to the belief that gas-solids drag reduction can be characterized by changes in the viscous sublayer. Only one previous theory, that of Jotaki and Tomita (ref. 10) has attempted to define a relationship between the sublayer thickness and the flow parameters of a dusty gas. However, their theory did not develop a relationship between changes in sublayer thickness and the amount of drag reduction. This relationship was developed during this study by extending and modifying the theory of Jotaki and Tomita to account for factors which were omitted in the original analysis. In the new form, the theory provided relationships between loading ratio, gas Reynolds number, and friction factor ratio which were in good agreement with the experimental results. This section includes a detailed description of the theory of Jotaki and Tomita and a detailed description of the modified theory.

Theory of Jotaki and Tomita

The following derivation for the thickness of the viscous sublayer in terms of suspension flow parameters was based on the work of Jotaki and Tomita. However, greater detail is reported here than was reported in the original paper (ref. 10). The Navier-Stokes equations were modified to include an additional Stokesian particle drag on the fluid:

$$\rho\left(\frac{\partial u_i}{\partial t} + u_\ell \frac{\partial u_i}{\partial x_\ell}\right) = -g_c \frac{\partial p}{\partial x_i} + \rho\nu \frac{\partial^2 u_i}{\partial x_\ell \partial x_\ell} + KN(v_i - u_i) \qquad (19)$$

$$i, \ell = 1,2,3$$

If the particles are small spheres:

$$K = 3\pi a \rho \nu \tag{20}$$

The continuity equation for the fluid was considered in its normal incompressible form:

$$\frac{\partial u_i}{\partial x_i} = 0 \tag{21}$$

Jotaki and Tomita assumed that the particles were so small that the local mean velocity of the gas and the particles were identical. At the same time, they assumed that the particles were still too large to respond at all to the turbulent fluctuations of the fluid.

Only that part of the mean flow distribution near the wall was considered. In turbulent flow, the velocity distribution within the viscous sublayer was represented by the linear law:

$$\frac{U}{U_*} = \frac{U_* x_2}{\nu} \quad \text{for} \quad \frac{U_* x_2}{\nu} \leq R_v \tag{22}$$

Farther from the wall, the velocity distribution was represented by the logarithmic law:

$$\frac{U}{U_*} = \frac{1}{K} \ln \frac{U_* x_2}{\nu} + B \quad \text{for} \quad \frac{U_* x_2}{\nu} \geq R_v \tag{23}$$

The value of the constants K (where K here is a Von Karman type constant) and B were determined by assuming a smooth variation in velocity profile at the edge of the viscous sublayer:

$$\left.\frac{d(U/U_*)}{d(U_*x_2/\nu)}\right|_{R_v} = 1$$

and (24)

$$\left.\frac{d(U/U_*)}{d(U_*x_2/\nu)}\right|_{R_v} = \left.\frac{1}{K(U_*x_2/\nu)}\right|_{R_v} = \frac{1}{KR_v} \quad \therefore K = \frac{1}{R_v}$$

Also:

$$\left.\frac{U}{U_*}\right|_{R_v} = R_v$$

and (25)

$$\left.\frac{U}{U_*}\right|_{R_v} = R_v \ell n R_v + B \quad \therefore B = R_v(1 - \ell n R_v)$$

The combination of the two laws, linear and logarithmic, gave:

$$\frac{U}{U_*} = R_v \ell n \frac{U_* x_2}{\nu} + R_v(1 - \ell n R_v) \tag{26}$$

Equation 26 gives an excellent description of the velocity profile in the sublayer and buffer zone.

The local fluid velocity was represented by:

$$u_i = U_i + u_i' + u_i'' \tag{27}$$

The local mean velocity, having a component only in the longitudinal direction, parallel to the wall, was described by equation 26. The fluctuating portion of the local fluid velocity was broken into two parts. The first part was characterized by the velocity components of a Townsend-Bakewell attached eddy in the sublayer:

$$u_1' = -u_2' = A\alpha^2 x_2 x_3 e^{-\frac{1}{2}\alpha^2(x_2^2 + x_3^2)} \tag{28}$$

$$u_3' = -A(1 - \alpha^2 x_2^2) e^{-\frac{1}{2}\alpha^2 (x_2^2 + x_3^2)} \tag{29}$$

Townsend (ref. 33) postulated the forms of these velocity components from measured correlations in pipe flow. The exponential variation provides the proper random nature and decay with distance. In the sublayer, these components represented the largest eddy components of the fluctuating velocity. The other part of the fluctuating velocity, u_i'', represented the smaller energy dissipative eddies in the sublayer and buffer zone.

Because the mean velocity profiles of the particles and the fluid were assumed identical, the difference between the two local velocities was given by:

$$v_i - u_i = -(u_i' + u_i'') \tag{30}$$

Assuming a steady mean flow, the Navier-Stokes equations became:

$$\frac{\partial}{\partial t}(u_i' + u_i'') + (U_\ell + u_\ell' + u_\ell'')\frac{\partial}{\partial x_\ell}(U_i + u_i' + u_i'')$$
$$= -\frac{g_c}{\rho}\frac{\partial}{\partial x_i}(P + p' + p'') + \nu \frac{\partial^2}{\partial x_\ell \partial x_\ell}(U_i + u_i' + u_i'') \tag{31}$$
$$- \frac{KN}{\rho}(u_i' + u_i'')$$

The particle number density, N, was assumed to be constant. In order to obtain the energy equation of the large eddy, equation 31 was multiplied by u_i':

$$u_i' \frac{\partial}{\partial t}(u_i' + u_i'') + u_i'(U_\ell + u_\ell' + u_\ell'')\frac{\partial}{\partial x_\ell}(U_i + u_i' + u_i'')$$

$$= -\frac{g_c u_i'}{\rho}\frac{\partial}{\partial x_i}(P + p' + p'') + u_i'\nu \frac{\partial^2}{\partial x_\ell \partial x_\ell}(U_i + u_i' + u_i'') \tag{32}$$

$$- u_i' \frac{KN}{\rho}(u_i' + u_i'')$$

Expanding the left hand side of equation 32 and noting that:

$$u_i' \frac{\partial}{\partial t}(u_i') + u_i' U_\ell \frac{\partial}{\partial x_\ell}(u_i')$$

$$= \frac{\partial}{\partial t}(\tfrac{1}{2}u_i'u_i') + U_\ell \frac{\partial}{\partial x_\ell}(\tfrac{1}{2}u_i'u_i') = \frac{d}{dt}(\tfrac{1}{2}u_i'u_i') \tag{33}$$

then:

$$\frac{d}{dt}(\tfrac{1}{2}u_i'u_i') + u_i' \frac{\partial u_i''}{\partial t} + u_i' \frac{\partial}{\partial x_\ell}\Big((u_i' + u_i'')(u_\ell' + u_\ell'')\Big)$$

$$+ u_i'U_\ell \frac{\partial U_i}{\partial x_\ell} + u_i'u_\ell'' \frac{\partial U_i}{\partial x_\ell} + u_i'u_\ell' \frac{\partial U_i}{\partial x_\ell} + u_i'U_\ell \frac{\partial u_i''}{\partial x_\ell}$$

$$= -\frac{g_c u_i'}{\rho}\frac{\partial}{\partial x_i}(P + p' + p'') + u_i'\nu \frac{\partial^2}{\partial x_\ell \partial x_\ell}(U_i + u_i' + u_i'') \tag{34}$$

$$- u_i' \frac{KN}{\rho}(u_i' + u_i'')$$

Equation 34 was simplified by noting that:

$$U_\ell \frac{\partial U_i}{\partial x_\ell} + \frac{\partial}{\partial x_\ell}(\overline{u_i u_\ell}) = -\frac{g_c}{\rho}\frac{\partial P}{\partial x_i} + \nu \frac{\partial^2 U_i}{\partial x_\ell \partial x_\ell} \tag{35}$$

$$\text{where } \overline{u_i u_\ell} = \overline{(u'_i + u''_i)(u'_\ell + u''_\ell)}$$

was the equation for the mean motion and by noting that

$$\frac{\partial U_\ell}{\partial x_\ell} = \frac{\partial u'_\ell}{\partial x_\ell} = \frac{\partial u''_\ell}{\partial x_\ell} = 0 \tag{36}$$

were the equations of continuity. Then:

$$\begin{aligned}
&\frac{d}{dt}(\tfrac{1}{2}u'_i u'_i) + u'_i \frac{\partial u''_i}{\partial t} + u'_i \frac{\partial}{\partial x_\ell}\left((u'_i + u''_i)(u'_\ell + u''_\ell) - \overline{u_i u_\ell}\right) \\
&\quad + u'_i u'_\ell \frac{\partial U_i}{\partial x_\ell} + u'_i \frac{\partial}{\partial x_\ell}(u''_i U_\ell + u''_\ell U_i) \\
&= -u'_i \frac{g_c}{\rho}\frac{\partial p'}{\partial x_i} - u'_i \frac{g_c}{\rho}\frac{\partial p''}{\partial x_i} + \nu\left[\frac{\partial}{\partial x_\ell}\left(u'_i \frac{\partial u'_i}{\partial x_\ell}\right) - \left(\frac{\partial u'_i}{\partial x_\ell}\right)\left(\frac{\partial u'_i}{\partial x_\ell}\right)\right] \\
&\quad - u'_i \frac{KN}{\rho}(u'_i + u''_i) + u'_i \nu \frac{\partial^2}{\partial x_\ell \partial x_\ell}(u''_i)
\end{aligned} \tag{37}$$

Equation 37 was integrated over all space (essentially over one Townsend-Bakewell eddy):

$$\begin{aligned}
-\int u'_i u'_\ell \frac{\partial U_i}{\partial x_\ell}\, dv &= \int u'_i \frac{\partial}{\partial x_\ell}\left((u'_i + u''_i)(u'_\ell + u''_\ell) - \overline{u_i u_\ell}\right) dv \\
&\quad + \nu \int \left(\frac{\partial u'_i}{\partial x_\ell}\right)\left(\frac{\partial u'_i}{\partial x_\ell}\right) dv + \frac{KN}{\rho}\int u'_i u'_i\, dv
\end{aligned} \tag{38}$$

Note that the terms:

$$\int u_i' \frac{\partial u_i''}{\partial t} dv, \quad \int u_i' \frac{\partial}{\partial x_\ell}(u_i'' U_\ell + u_\ell'' U_i)\, dv, \quad \frac{KN}{\rho} \int u_i' u_i'' dv,$$

$$-\int u_i' \frac{g_c}{\rho} \frac{\partial p''}{\partial x_i} dv, \quad \text{and} \quad \int u_i' \nu \frac{\partial^2}{\partial x_\ell \partial x_\ell}(u_i'')\, dv$$

were dropped because the scales of the large eddies and the small eddies were assumed not to be correlated. Space integrals of products of large scale and small scale fluctuations would be negligible.

The terms $-\frac{g_c}{\rho} \int u_i' \frac{\partial p'}{\partial x_i} dv$ and $\nu \int \left(\frac{\partial}{\partial x_\ell} \left(u_i' \frac{\partial u_i'}{\partial x_\ell} \right) \right) dv$ were dropped because the flow field was bounded and the flow of turbulent energy vanished at the wall. The term $g_c/\rho \int u_i' \frac{\partial p'}{\partial x_i} dv$ can be transformed, using the divergence theorem, into:

$$\frac{g_c}{\rho} \int u_i' \frac{\partial p'}{\partial x_i} dv = \frac{g_c}{\rho} \int u_2' p' ds - \frac{g_c}{\rho} \int p' \frac{\partial u_i'}{\partial x_i} dv \tag{39}$$

$\frac{g_c}{\rho} \int u_2' p' ds$ vanished because $u_2' p'$ was zero at the surface (the divergence theorem requires that only the normal component to the surface, u_2', be considered in the surface integral), and $\frac{g_c}{\rho} \int p' \frac{\partial u_i'}{\partial x_i} dv$ vanished because of continuity. The term $\nu \int \frac{\partial}{\partial x_\ell} \left(u_i' \frac{\partial u_i'}{\partial x_\ell} \right) dv$ can be transformed:

$$\nu\int \frac{\partial}{\partial x_\ell}\left(u_i' \frac{\partial u_i'}{\partial x_\ell}\right) dv = \nu\int \left(\frac{\partial u_i'}{\partial x_\ell}\right)\left(\frac{\partial u_i'}{\partial x_\ell}\right) dv + \nu\int u_i' \frac{\partial^2 u_i'}{\partial x_\ell \partial x_\ell} dv$$

$$= \nu\int \left(\frac{\partial u_i'}{\partial x_\ell}\right)\left(\frac{\partial u_i'}{\partial x_\ell}\right) dv + \nu\int \frac{\partial^2}{\partial x_\ell \partial x_\ell}\left(\tfrac{1}{2} u_i' u_i'\right) dv \qquad (40)$$

$$- \nu\int \left(\frac{\partial u_i'}{\partial x_\ell}\right)\left(\frac{\partial u_i'}{\partial x_\ell}\right) dv$$

The remaining term $\nu\int \frac{\partial^2}{\partial x_\ell \partial x_\ell}(\frac{1}{2} u_i' u_i')dv$ was identically zero:

$$\nu\int \frac{\partial^2}{\partial x_\ell \partial x_\ell}\left(\tfrac{1}{2} u_i' u_i'\right) dv = \nu\int \frac{\partial}{\partial x_2}\left(\tfrac{1}{2} u_i' u_i'\right) ds = \nu\int \frac{\partial}{\partial x_2}\left(\tfrac{1}{2} u_3'^2\right) ds \qquad (41)$$

which vanished at the surface (again considering only the normal component and also that $u_1' = u_2' = 0$ at the surface).

The term $\frac{d}{dt}\int \frac{1}{2} u_i' u_i' dv$ was dropped from equation 37 because it was assumed that the large eddy was in a state of equilibrium. Equation 38, therefore, represented an integral energy balance for the Townsend-Bakewell eddy. The gain of energy from the mean flow, the left hand side of the equation was exactly balanced by the three part dissipation on the right hand side of the equation. The dissipation was composed of (1) energy loss to the smaller eddies (additional Reynolds stress), (2) direct viscous dissipation, and (3) additional dissipation produced by the presence of particles. The additional Reynolds stress was calculated from:

$$\overline{u_i u_\ell} - (u_i' + u_i'')(u_\ell' + u_\ell'') = 2\nu_T S_{i\ell}' \qquad (42)$$

where $\nu_T = \frac{x_2 U_*}{R_Y}$. The diagonal components of $S_{i\ell}'$ were ignored (ref. 33) so that:

$$S'_{i\ell} = \begin{bmatrix} 0 & \frac{1}{2}\left(\frac{\partial u'_2}{\partial x_1} + \frac{\partial u'_1}{\partial x_2}\right) & \frac{1}{2}\left(\frac{\partial u'_3}{\partial x_1} + \frac{\partial u'_1}{\partial x_3}\right) \\ S_{12} & 0 & \frac{1}{2}\left(\frac{\partial u'_3}{\partial x_2} + \frac{\partial u'_2}{\partial x_3}\right) \\ S_{13} & S_{23} & 0 \end{bmatrix} \qquad (43)$$

All of the terms in equation 38 were defined, so that it was possible to complete the integration of equation 38. The limits of the integrals were 0 to 1 for x_1, 0 to infinity for x_2, and negative infinity to positive infinity for x_3.

The integration of the left-hand side of equation 38 was straightforward. Because it illustrates the mathematics, it will be shown below in detail:

$$-\int u'_i u'_\ell \frac{\partial U_i}{\partial x_\ell} dv = -\int_0^1 \int_{-\infty}^{\infty} \int_0^{\infty} u'_1 u'_2 \frac{\partial U_1}{\partial x_2} dx_2 dx_3 dx_1$$

$$= 2\int_0^1 \int_0^{\infty} \int_0^{\infty} \frac{R_v U_*}{x_2} A^2 \alpha^4 x_2^2 x_3^2 e^{-\alpha^2 x_2^2} e^{-\alpha^2 x_3^2} \; dx_2 dx_3 dx_1$$

$$= 2R_v U_* A^2 \alpha^4 \int_0^1 dx_1 \int_0^{\infty} x_2 e^{-\alpha^2 x_2^2} dx_2 \int_0^{\infty} x_3^2 e^{-\alpha^2 x_3^2} dx_3 \qquad (44)$$

$$= 2R_v U_* A^2 \alpha^4 (1) \left(\frac{1}{2\alpha^2}\right)\left(\frac{1}{4\alpha^2} \sqrt{\frac{\pi}{\alpha^2}}\right) = \frac{\sqrt{\pi} \; A^2 U_*}{4\alpha} R_v$$

The integration of the right-hand side involved multiple use of the exponential integral formulas and was extremely lengthy because of the many summations, differentiations, and multiplications required.

The integration will be shown below in outline form only. For the Reynolds stress term:

$$\int u_i' \frac{\partial}{\partial x_\ell}\left((u_i' + u_i'')(u_\ell' + u_\ell'') - \overline{u_i u_\ell}\right)dv$$

$$= \int u_i' \frac{\partial}{\partial x_\ell}\left(2\frac{U_* x_2}{R_v} S_{i\ell}'\right)dv \tag{45}$$

$$= -4\,\frac{U_*}{R_v}\int_0^\infty \int_0^\infty u_i' \frac{\partial}{\partial x_\ell}(x_2 S_{i\ell}')\,dx_2 dx_3$$

This term was simplified by noting that the diagonal terms of the strain tensor were to be ignored and that the u_i' were not functions of x_1.

$$\therefore\ -4\,\frac{U_*}{R_v}\int_0^\infty \int_0^\infty u_i' \frac{\partial}{\partial x_\ell}(x_2 S_{i\ell}')\,dx_2 dx_3$$

$$= -4\frac{U_*}{R_v}\int_0^\infty \int_0^\infty \left[u_1' \frac{\partial}{\partial x_2}(x_2 S_{12}') + u_1' \frac{\partial}{\partial x_3}(x_2 S_{13}') + u_2' \frac{\partial}{\partial x_3}(x_2 S_{23}') + u_3' \frac{\partial}{\partial x_2}(x_2 S_{32}')\right]dx_2 dx_3 \tag{46}$$

After substitution of the strain tensor components and the equations for the large eddy velocity components and after completing the integration, the Reynolds stress term became:

$$\frac{U_* A^2}{\alpha R_v}\sqrt{\pi}\frac{1}{4} + \frac{U_*}{\alpha}\frac{A^2}{R_v}\sqrt{\pi}\,\frac{3}{8} + \frac{U_* A^2}{\alpha R_v}\sqrt{\pi}\,\frac{1}{8} + \frac{U_* A^2}{\alpha R_v}\sqrt{\pi}\,\frac{10}{8}$$

$$= 2\sqrt{\pi}\;\frac{A^2 U_*}{\alpha R_v} \tag{47}$$

For the viscous dissipation term:

$$\nu\int\left(\frac{\partial u_i'}{\partial x_\ell}\right)\left(\frac{\partial u_i'}{\partial x_\ell}\right)dv \quad = 2\nu\int_0^\infty\int_0^\infty \left(\frac{\partial u_i'}{\partial x_\ell}\right)\left(\frac{\partial u_i'}{\partial x_\ell}\right)dx_2dx_3$$

$$= 2\nu\int_0^\infty\int_0^\infty \left[\left(\frac{\partial u_1'}{\partial x_2}\right)\left(\frac{\partial u_1'}{\partial x_2}\right) + \left(\frac{\partial u_1'}{\partial x_3}\right)\left(\frac{\partial u_1'}{\partial x_3}\right)\right.$$

$$+ \left(\frac{\partial u_2'}{\partial x_2}\right)\left(\frac{\partial u_2'}{\partial x_2}\right) + \left(\frac{\partial u_2'}{\partial x_3}\right)\left(\frac{\partial u_2'}{\partial x_3}\right) \tag{48}$$

$$\left. + \left(\frac{\partial u_3'}{\partial x_2}\right)\left(\frac{\partial u_3'}{\partial x_2}\right) + \left(\frac{\partial u_3'}{\partial x_3}\right)\left(\frac{\partial u_3'}{\partial x_3}\right)\right]dx_2dx_3$$

After substitution of the large eddy velocity components, the viscous dissipation term became:

$$\frac{3}{16}\pi\nu A^2 + \frac{3}{16}\pi\nu A^2 + \frac{3}{16}\pi\nu A^2 + \frac{3}{16}\pi\nu A^2$$

$$+ \frac{15}{16}\pi\nu A^2 + \frac{3}{16}\pi\nu A^2 = \frac{15}{8}\pi\nu A^2 \tag{49}$$

For the particle dissipation term:

$$\frac{KN}{\rho}\int u_i'u_i'dv = 2\frac{KN}{\rho}\int_0^1\int_0^\infty\int_0^\infty (u_1'u_1' + u_2'u_2' + u_3'u_3')dx_2dx_3dx_1 \tag{50}$$

$$= 2\frac{KN}{\rho}\int_0^\infty\int_0^\infty A^2 e^{-\alpha^2(x_2^2 + x_3^2)}(2\alpha^4x_2^2x_3^2 + 1 - 2\alpha^2x_2^2 + \alpha^4x_2^4)dx_2dx_3$$

$$= 2\frac{KN}{\rho}\left[\frac{A^2\pi}{16\alpha^2} + \frac{A^2\pi}{16\alpha^2} + \frac{3A^2\pi}{16\alpha^2}\right] = \frac{5\pi}{8}\,\frac{KN}{\rho}\,\frac{A^2}{\alpha^2}$$

The final result of the full integration was:

$$\frac{\sqrt{\pi}A^2U_*}{4\alpha}R_v = \frac{2\sqrt{\pi}\,A^2U_*}{\alpha R_v} + \frac{15}{8}\pi\nu A^2 + \frac{5\pi}{8}\,\frac{KN}{\rho}\,\frac{A^2}{\alpha^2} \tag{51}$$

Assuming:

$$\frac{1}{\alpha} = \delta_v \tag{52}$$

and noting that:

$$\eta = \frac{\pi}{6}a^3N\frac{\rho_p}{\rho},\quad t_R = \frac{1}{18}\,\frac{a^2}{\nu}\,\frac{\rho_p}{\rho},\quad \text{and}\quad \frac{KN}{\rho} = \frac{\eta}{t_R}$$

for equal particle and air bulk average velocities, equation 51 was solved explicitly for the dimensionless sublayer thickness:

$$R_v = \sqrt{\frac{8\left(1 + \frac{15}{16}\sqrt{\pi}\right)}{\left(1 - \frac{5\sqrt{\pi}}{2}\,\frac{\nu}{U_*^2}\,\frac{\eta}{t_R}\right)}} \tag{53}$$

Jotaki and Tomita did not use equation 53 to establish a relationship between sublayer thickness and the amount of drag reduction. They did use the assumptions of their analysis to determine the conditions for which drag reduction could be expected. Use of the Stokes drag formula required that the particle Reynolds number be less than unity:

$$\frac{(u_i' + u_i'')a}{\nu} \approx \frac{2aU_*}{\nu} < 1 \tag{54}$$

The assumption that the particles had no fluctuating component of velocity required that the relaxation time of the particles be longer than the characteristic time of the flow in the wall region:

$$\frac{1}{18}\frac{a^2}{\nu}\frac{\rho_p}{\rho} > \frac{\nu}{U_*^2} \qquad (55)$$

The assumption that the mean particle velocity be the same as the mean gas velocity required that the terminal velocity of the particles be smaller than the characteristic velocity of the flow in the wall region:

$$\frac{1}{18}\frac{a^2}{\nu}\frac{\rho_p}{\rho} g < U_* \qquad (56)$$

Combination of the equations 54 through 56 and the additional requirement that R_v in equation 53 be real gave the following requirements for flow parameters in a drag reducing suspension:

$$\eta < \frac{1}{180\sqrt{\pi}}\frac{\rho_p}{\rho} \qquad (57)$$

$$\frac{\rho}{\rho_p} < \frac{1}{72} \qquad (58)$$

$$a < \frac{1}{2}\sqrt[3]{\nu^2/g} \qquad (59)$$

For glass beads in air, the inverse of the density ratio is 2130. The maximum loading ratio and bead size for drag reduction would therefore be 6.68 and 142μ respectively. These values are reasonable and include the range of parameters investigated here and in most other studies. However, some investigators have reported drag reduction with higher loading ratios and larger particle sizes. Jotaki and Tomita indicated that the conditions of equations 57 through 59 may be too restrictive. They felt that drag reduction would occur as long as the additional dissipation produced by the presence of particles outweighed any additional turbulent energy production (produced possibly by disturbances from large particle wakes or by an increased effective fluid density).

Modification and Extension of the Theory of Jotaki and Tomita

Jotaki and Tomita did not develop a relationship between the dimensionless sublayer thickness, R_V, and the friction factor. This relationship was obtained using the combined velocity profile of the viscous sublayer and buffer layer (equation 26) and the relationship:

$$U_* = U\sqrt{\frac{f}{8}} \qquad \text{or } f = 8\left(\frac{U_*}{U}\right)^2 \tag{60}$$

where U was the bulk average gas velocity and was a constant for a given gas Reynolds number. (Note that U in equation 26 was the local mean velocity which varied continuously from the wall.)

In order to use the velocity profile (equation 26) as a relationship between R_V and U_*, a point of the buffer layer velocity profile was required. This point was available from the experimentally measured velocity profiles. In particular, the traverse point nearest the wall was within the buffer layer. Using the velocity here, equation 26 defined the variation of R_V with U_*. The basic assumption of this newly defined relationship was that the presence of particles did not destroy the validity of the logarithmic law. This assumption had been well justified by the suspension air velocity profiles.

Figure 18 shows the relationship of R_V and U_* calculated for Reynolds numbers of 12,000; 18,000; and 22,000. The values of R_V corresponding to the values of U_* determined by the clean gas pressure drop measurements are shown by the dashed curve. The curve has been extended to a Reynolds number of 50,000 using a value of U_* calculated from the experimental friction factor correlation. In the range $12,000 < Re_g < 50,000$, the value of R_v is seen to vary only slightly for the clean gas. At a Reynolds number of 18,000, the value of R_v (4.61) predicted theoretically by equation 53 for the clean gas was in exact correspondence with the value of R_v calculated from the experimental data and equation 26.

Figure 18 showed that larger dimensionless sublayers produced smaller friction velocities (and therefore friction factors) and confirmed analytically that thickened sublayers can cause drag reduction. On the one hand, the figure showed that the amount of drag reduction was limited as the sublayer thickened to the order of quadruple the original thickness. On the other hand, the amount of drag increase by sublayer thinning was not limited.

Figure 19 shows the information of figure 18 recast in the form of friction factor ratio versus dimensionless sublayer thickness ratio for the range of Reynolds numbers considered in this study. In this form, the figure showed that the friction factor ratio was a very weak function of Reynolds number, in exact correspondence with the experimental results. The amount of drag reduction was limited to about 50 percent for reasonable values of the dimensionless sublayer thickness ratio. This was also in accordance with the experimental results.

Because the friction factor ratio was essentially independent of Reynolds number, as shown in figure 19, a theoretical prediction of the amount of drag reduction needed to consider only one consistent set of values of R_v and U_*. The exact correspondence of the theoretically and experimentally derived values of R_v for a Reynolds number of 18,000 obliged the use of this set of values.

Equation 53 and Figure 19 were used to compare the experimentally measured amounts of drag reduction for a particular loading ratio and particle size with theoretical predictions. Equation 53 provided an unsatisfactory prediction as theoretical loading ratios in excess of those considered valid by the assumptions of the analysis were required to produce the amount of sublayer thickening indicated by the experiments. Consequently, the analysis was modified to account for two factors, the first enhancing drag reduction, the second limiting drag reduction, which were not considered in the original analysis. The two factors were both related to the most questionable assumption in the Jotaki and Tomita analysis: that the particles were at the same time completely responsive to the mean flow and totally unresponsive to the turbulent fluctuations of the gas.

The first factor, c_1, was introduced into the final term of equation 19 to correct the relative velocity between the solids and the gas. The factor represented the ratio between the velocity of the particles at the wall (which do not follow the no-slip boundary condition) and the characteristic velocity of the Townsend-Bakewell eddy. The factor could be interpreted in two ways. First it accounted for the higher actual relative velocity and increased dissipation between the two phases in the near wall region. Second, it represented the effectively higher loading ratio in the thin sublayer region because the particles were travelling faster than the gas.

According to Bakewell and Lumley (ref. 34), the characteristic velocity of the large eddy was:

$$A \approx 0.7U_* \tag{61}$$

Reddy and Pei (ref. 31) suggested that the particle velocity at the wall could be estimated by:

$$V_{pw} = V_{pc}\left(\frac{a}{D}\right)^{1/n} \tag{62}$$

The value of n, calculated from the data of Reddy and Pei was 10.42 for 200μ particles. Extrapolating this value from the data of Reddy and Pei with 100μ, 150μ, 200μ, and 270μ particles to the 36.0μ particles used here gave a value of 9.38 for n. Equation 62 therefore gave a value of V_{pw} of 25.25 ftsec^{-1} for the #380 glass beads at a Reynolds number of 18,000 in the 0.870 inch inside diameter tube.

In the 1 inch inside diameter glass tube, the particle velocities measured nearest the wall (the camera was actually focused at the wall) were of the order of 21 ftsec^{-1} for tube centerline velocities of 37.5 ftsec^{-1} which was considered as the equivalent of 28 ftsec^{-1} for tube centerline velocities of 50 ftsec^{-1} (corresponding to a Reynolds number of 18,000) in the 0.870 inch inside diameter tube. The particle velocity measured nearest the wall was considered as an upper estimate for the velocity at the wall since the depth of field of the camera was thicker than the viscous sublayer. Because the camera was focused at the wall, this estimate was probably close to the actual velocity at the wall.

Therefore using the Reynolds number of 18,000 in the 0.870 inch inside diameter tube, the factor c_1 was chosen as

$$c_1 = \frac{V_{pw}}{A} \approx \frac{25.25}{0.7U_*} = \frac{25.25}{0.7(2.38)} = 15.15 \approx 15$$

Unfortunately experimental data was not available to estimate c_1 for the #279 and #980 glass beads. However c_1 was estimated as 5.40 and 2.60 for the #279 and #980 glass beads by considering the relative settling velocities of the various glass bead sizes. The relative settling velocities were assumed to be the best measure of the relative response of the particles to the mean flow and therefore were used for the extrapolation of c_1 to very small particle sizes.

The second factor, c_2, was introduced in order to account for the proportionate increase in turbulent production produced by the presence of particles. Calculations of the response of a particle to a given turbulent spectrum (homogeneous and isotropic) have been made and reported (ref. 7). In the work reported by Soo, the response of 50 micron and 5 micron carbon particles to a given turbulent air spectrum corresponding to the centerline of a pipe was calculated. The results were plotted in terms of relative energy, compared to the energy of the air at a frequency of 10 cyclessec^{-1}, versus frequency. The area under the energy-frequency curve was a measure of the turbulence intensity. The area under the curve for the 50 micron particles was 0.082 of the area under the curve for the air indicating that the particles were effectively responsive to 8.2% of air turbulence. For high frequencies, which are typical of the turbulence near the wall, the smaller 5 micron particles were two orders of magnitude more responsive than the 50 micron particles.

In order to estimate c_2 for the #380 glass beads in the near wall region, the response of the 50μ carbon particles to the air turbulence at the center of a pipe was used as a base point. The relative response of the 50μ and 5μ particles to the small eddies or high frequency turbulence implied that the response was, roughly, inversely proportional to the square of the particle diameter. This suggested that the #380 glass beads would be effectively responsive to $(\frac{50}{36})^2$ (0.082) or 0.162 of the air turbulence provided the scale of the average eddy at the centerline was the same as that in the near wall region.

However, the scale of the average eddy was much smaller near the wall than at the centerline. A measure of the relative average eddy size between the pipe centerline and the near wall region was provided by the relative magnitude of the mixing length between the pipe centerline and the near wall region. From previous investigations (ref. 13), the mixing length in the region $y/R < 0.1$ is one order of magnitude smaller than at the pipe centerline. Therefore, scaling the factor c_2 by the relative size of the average eddy gave a value of 0.0162 for the #380 glass beads. Because the approximation was crude, c_2 was rounded to 0.02 for the #380 glass beads. The magnitude of c_2 for the other particle sizes was scaled by the squares of the particle diameter, therefore c_2 was chosen as 0.056 and 0.115 for the #279 and #980 glass beads respectively. Therefore an equal (to the gas flow rate) flow rate of #380 glass beads was considered to add only another 2 percent to the turbulent production of the gas. The #980 glass beads, being so much smaller and more responsive to the flow, were considered to add another 11.5 percent to the turbulent production of the gas.

The factor, c_2, was included in equation 19 by multiplying the density of the fluid by $1 + c_2\eta$. Equation 19 with c_1 and c_2 included became:

$$\rho(1 + c_2\eta)\left(\frac{\partial u_i}{\partial t} + u_\ell \frac{\partial u_i}{\partial x_\ell}\right) = -g_c \frac{\partial p}{\partial x_i} + \rho(1+c_2\eta)\nu \frac{\partial^2 u_i}{\partial x_\ell \partial x_\ell} + c_1 KN(v_i - u_i) \qquad (63)$$

The integration of this equation followed as before so that the equation for R_v became:

$$R_v = \sqrt{\frac{8\left(1 + \frac{15}{16}\frac{\sqrt{\pi}}{1 + c_2\eta}\right)}{1 - \frac{5\sqrt{\pi}}{2}\frac{\nu}{U_*^2}\frac{\eta}{t_R}\frac{c_1}{1 + c_2\eta}}} \qquad (64)$$

Equation 64 and figure 19 were used to calculate the results shown on figure 20 where friction factor ratio is plotted versus loading ratio for the #380 glass beads with $c_1 = 15$ and two values of c_2.

The sensitivity of the solution to small changes in the value of c_2 of the order of 0.1 is readily apparent. Changing the turbulent production factor c_2 from 0 to 0.1 has the effect of increasing the loading ratio for a given amount of drag reduction by about 40 percent. The figure implied that if c_2 were increased to values near unity little drag reduction could be expected at reasonable values of loading ratio.

Figure 21 shows the theoretical prediction of friction factor ratio versus loading ratio for the #980, #279, and #380 glass beads. The agreement with the experimental results (Figures 7 and 8) is quite good. At the highest values of loading ratio, the limiting value of drag reduction observed experimentally could be predicted adequately by assuming a very small additional bulk slip velocity of the order of 25 percent of the particle terminal settling velocity. For example, equation 65 (taken from ref. 36 and given below) was used to show that a bulk average particle slip velocity only 27% greater than the particle terminal settling velocity could increase the friction factor ratio of the #380 glass bead suspension by 15 percent. This result is shown on figure 21 and brings the theoretically predicted curve into close agreement with the experimental data.

$$\Delta P_{dds} = \frac{LW_p}{AV_p}\left(1 - \frac{\rho_t}{\rho_p}\right)\left(\frac{\rho}{\rho_t}\right)\left(\frac{U - \mathbf{V}_p}{V_t}\right)^2 \frac{g}{g_c} \qquad (65)$$

The bulk average particle slip velocity could be expected to increase at higher loading ratios and particle number densities because of increased particle-particle and particle-wall impacts. The small additional slip velocity, only 0.088 ftsec^{-1} for the #380 glass beads, was well within the precision limits of the particle velocity measurement system.

Conclusions

An investigation into the existence, causes, and effects of gas-solids drag reduction was performed in a recirculating closed loop system. Pressure drop measurements were made on suspensions flowing in vertical and horizontal 0.870 inch, inside diameter, tubes. Profile measurements were made only on suspensions flowing in the vertical tube. The measurements included data, in the presence of particles, on gas friction factors, gas velocity profiles, gas turbulence intensity profiles, gas turbulent spectra, and particle velocity profiles. Five glass bead sizes ranging from 10 to 60 micron diameter were suspended in air at gas Reynolds numbers of 10,000 to 25,000 and solids loading ratios from 0 to 4.

The investigation led to the following important observations, results, and conclusions:

1. The five glass bead designations #980 (15.0 micron diameter), #981 (21.0 micron diameter), #279 (21.6 micron diameter), #380 (36.0 micron diameter), #660 (55.0 micron diameter), were sized before and after circulation in the closed loop system and were found, with the exception of the #660 glass

beads, to retain their initial weight mean diameter. The #660 glass beads suffered a three-fold reduction in average size, apparently a consequence of prolonged passage through the pump.

2. A sharp-edged orifice was used to measure the gas mass flow rate independently of the solids flow rate. The orifice calibration for the clean gas flow was found to be valid for gas flow containing dilute volumetric concentrations of solids.
3. A target-meter was used in conjunction with the sharp-edged orifice to determine the solids flow rate in the closed loop. The signal from strain gauges mounted on the target-meter support was found to be linear with the force of gas and solids striking the target. The response of the target-meter, determined during an open loop calibration, was dependent upon the size of the impacting particles.
4. Clean air friction factors were independent of the test section orientation and were in excellent agreement with accepted correlations.
5. A fiber-film probe was used to measure gas turbulence quantities in suspension flow. The fiber-film registered approximately 60 to 70 percent of the turbulence registered by a hot wire, was only slightly temperature sensitive, and withstood the bombardment of particles for a considerable length of time.
6. The clean air velocity profiles were in excellent agreement with the universal velocity profile. The profiles carried from the centerline of the tube to the outside edge of the buffer layer.
7. Measurements of the clean air turbulence profiles agreed with

published results on the direction of increased turbulence intensity as probe locations and gas Reynolds numbers were varied. The turbulence intensity relative to the local mean velocity increased from the tube centerline, slowly at first, and then rapidly as the wall was approached. The turbulence intensity relative to the local mean velocity at a fixed radial position decreased with increased values of Reynolds number.

8. The spectrum analyses indicated that the fiber-film probe had relatively little sensitivity to small eddies.
9. Large particles permitted circulation of higher loading ratios than small particle sizes. Larger Reynolds numbers also permitted circulation of higher loading ratios, although the Reynolds number effect was not as important or as consistent as the particle size effect.
10. Electrostatically induced deposition was important only for the #980 glass beads. Deposition induced by thermophoresis was observed on the cool wall of the water jacketed section. The tendency toward deposition increased with decreasing particle size because of agglomeration. Large individual particles were less prone to leave the main flow pattern.
11. Drag reduction was achieved for all five glass bead designations in the vertical test section. The maximum drag reduction was about 40% for both the #380 and #660 glass beads. The onset of drag reduction with loading ratio was progressively delayed with increasing particle size. The drag reduction was only a weak function of gas Reynolds number. The results for the #380 glass beads indicated that an optimum loading ratio existed for the maximum amount of

drag reduction.

12. Drag reduction was achieved for the three smallest glass bead sizes in the horizontal test section. The results were almost identical to the results obtained in the vertical test section for the #980, #981, and #279 glass beads. The #380 and #660 glass bead suspensions yielded drag increases rather than drag reduction. Apparently gravity segregation and sedimentation had a negligible effect upon the drag reducing ability of the smaller particle sizes but had a detrimental effect upon that of the larger particle sizes.
13. The suspension air velocity profiles were similar to the corresponding clean air velocity profiles. The suspension profiles, when recast in terms of the friction velocity and the universal velocity profile, indicated that drag reduction was caused by a thickening of the viscous sublayer and the buffer layer.
14. The suspension air turbulence intensity profiles all indicated that the presence of particles had the effect of increasing the air turbulence above the clean air values. The results, when normalized with friction velocity and plotted against the non-dimensional distance to the wall, enforced the conclusion that drag reduction in a gas-solids suspension could be characterized by a thickening of the viscous sublayer. There was no general turbulence suppression.
15. The particle velocity profiles were, within experimental accuracy of the double flash photographic technique, the same as the air velocity profiles with the exception of a finite slip velocity at the wall. The results indicated that a continuum approach, predicting bulk slip velocities much larger than terminal settling velocities, was invalid to

to describe the suspension profiles.

16. The drag reduction results could be predicted theoretically by calculating the effect of particles on the Townsend-Bakewell eddy structure in the viscous sublayer. The particles have the effect of interfering with the equilibrium energy transfer between the Townsend-Bakewell eddies and the smaller energy dissipative eddies in the near wall region. Provided the particles do not produce excessive inertial effects, the particles can produce a thickened viscous sublayer and reduce the shear stress.

List of Symbols

a	particle diameter, ft.
A	flow cross-section in equation 65, ft^2.
A	characteristic velocity of attached eddy in equations 28, 29, 44, 47, 49, 50, 51, and 61, $ftsec^{-1}$.
A_p	pipe flow cross section, ft^2.
A_T	mass flowmeter target area, ft^2.
B	constant in equations 23 and 25, dimensionless.
c_1	ratio of particle slip velocity at wall to characteristic velocity A of attached eddy, dimensionless.
c_2	effective proportion of particles contributing to turbulent production, dimensionless.
C_D	target drag coefficient, dimensionless.
D	pipe inside diameter, ft.
f	general Blasius friction factor, dimensionless.
f_g	Blasius friction factor of clean gas, dimensionless.

f_s	Blasius friction factor of suspension based on gas properties, dimensionless.
F	total force on target, lbf.
F_g	force of gas on target, lbf.
F_p	force of particles on target, lbf.
g	gravitational acceleration, ftsec^{-2}.
g_c	gravitational constant, ftlbmlbf^{-1}sec^{-2}.
K	Von Karman type constant in equations 23 and 24, dimensionless.
K	Stokes drag parameter in equations 19, 20, 31, 32, 34, 37, 38, 50, 51, and 63, lbmsec^{-1}.
L	length of test section in equations 15, 17, and 65, ft.
n	factor in equation 62, dimensionless.
N	particle number density, ft^{-3}.
p	local pressure, lbfft^{-2}.
p'	large eddy component of pressure, lbfft^{-2}.
p"	small eddy component of pressure, lbfft^{-2}.
P	local mean pressure, lbfft^{-2}.
P_{ads}	pressure related to acceleration of dispersed solids, lbfft^{-2}.
P_{ag}	pressure related to acceleration of gas, lbfft^{-2}.
P_{dds}	pressure related to drag of particles, lbfft^{-2}.
P_f	pressure related to combined friction of gas and dispersed solids, lbfft^{-2}
P_{fds}	pressure related to friction of dispersed solids, lbfft^{-2}.

P_{fg}	pressure related to friction of gas, lbfft^{-2}.
P_{Lds}	pressure related to static head of dispersed solids, lbfft^{-2}.
P_{Lg}	pressure related to static head of gas, lbfft^{-2}.
r	radial coordinate, ft.
R	radius of pipe, ft.
R_v	dimensionless sublayer thickness, dimensionless.
R_{vg}	dimensionless sublayer thickness for the clean gas, dimensionless.
Re_g	$UD\nu^{-1}$, Reynolds number based upon gas properties, dimensionless.
s	surface area, ft^2.
$S'_{i\ell}$	large eddy component of strain rate, sec^{-1}.
t	time, sec.
t_R	Stokesian particle relaxation time, sec.
u	local velocity, ftsec^{-1}.
u_i, u_ℓ	component of local velocity, ftsec^{-1}.
u'_i, u'_ℓ	component of velocity fluctuation caused by large eddy, ftsec^{-1}.
u''_i, u''_ℓ	component of velocity fluctuation caused by small eddy, ftsec^{-1}.
U	local mean velocity, ftsec^{-1}.
U	bulk average gas velocity in equations 2-8, 17, 60, 65, and definition of Re_g, ftsec^{-1}.
$U_c, U_{℄}$	local mean velocity at centerline, ftsec^{-1}.
U_i, U_ℓ	component of local mean velocity, ftsec^{-1}.

U_*	$(g_c\ \tau_w \rho^{-1})^{\frac{1}{2}}$, friction velocity, ftsec^{-1}.
v	volume in equations 38 - 41, 44 -45, 48, and 50, ft^{3}.
v_i	local particle velocity, ftsec^{-1}.
V_p	bulk average particle velocity, ftsec^{-1}.
V_{pc}	particle centerline velocity, ftsec^{-1}.
V_{pcs}	particle centerline slip velocity, ftsec^{-1}.
V_{ps}	bulk average particle slip velocity, ftsec^{-1}.
V_{pw}	particle slip velocity at wall, ftsec^{-1}.
V_t	particle terminal settling velocity, ftsec^{-1}.
V_{ST}	recorder output voltage, mv.
V_{STO}	recorder output voltage for gas flow only, mv.
W_g	mass flow rate of gas only, lbmsec^{-1}.
W_p	mass flow rate of particles only, lbmsec^{-1}.
x_i, x_ℓ	general coordinate, ft.
x_1	longitudinal coordinate, ft.
x_2	transverse coordinate, ft.
x_3	spanwise coordinate, ft.
y	x_2, distance from pipe wall, ft.
y^*	$yU_*\nu^{-1}$, dimensionless distance from pipe wall, dimensionless.
α	parameter of Townsend attached eddy, ft^{-1}.
δ_v	thickness of viscous sublayer, ft.
η	$W_p W_g^{-1}$, loading ratio, dimensionless.

μ	micron
μ	gas viscosity, lbmft^{-1}sec^{-1}.
ν	$u\rho^{-1}$, gas kinematic viscosity, ft^{2}sec^{-1}.
ν_T	eddy kinematic viscosity, ft^{2}sec^{-1}.
ρ	gas density, lbmft^{-3}.
ρ_{ds}	dispersed solids density, lbmft^{-3}.
ρ_p	density of a particle, lbmft^{-3}.
ρ_t	density of fluid in which particle terminal settling velocity is measured, lbmft^{-3}.
τ_w	wall shear stress, lbfft^{-2}.

References

1 Kane, R.S. 1973. Drag reduction in dilute flowing gas-solids suspensions. Ph.D. Thesis, City University of New York.

2 Rossetti, S.J. 1969. Experimental determination of pressure drop and flow characteristics of dilute gas-solid suspensions. Ph.D. Thesis, City University of New York.

3 Pfeffer, R. and Rossetti, S.J. 1971. Experimental determination of pressure drop and flow characteristics of dilute gas-solid suspensions. NASA CR-1894.

4 Sproull, W.T. 1961. Viscosity of dusty gases. Nature, <u>190</u>, 976-978.

5 Owen, P.R. 1969. Pneumatic transport. J. Fluid Mech., <u>39</u>, 407-432.

6 Richardson, J.F. and McCleman, M. 1960. Pneumatic conveying - Part II Solids velocities and pressure gradients in a one-inch horizontal pipe. Trans. Instn. Chem. Engrs., <u>38</u>, 257-266.

7 Soo, S.L. 1967. Fluid Dynamics of Multiphase Systems. Waltham: Blaisdell Publishing Co.

8 Peskin, R.L. and Dwyer, H.A. 1964. A study of the mean flow characteristics of gas-solid suspensions. Technical Report No. 101-ME-F, Dept. of Mech. Engng., Rutgers University.

9 Lumley, J.L. 1964. The reduction of skin friction drag. Fifth Symposium on Naval Hydrodynamics, Bergen, Norway, 915-946.

10 Jotaki, T. and Tomita, Y. 1971. Turbulent friction drag of a dusty gas. Paper C5, Proc. 1st. Int. Conf. on Pneumatic Transport of Solids in Pipes, BHRA Fluid Engng., Cranfield, U.K. (September 1971).

11 Boothroyd, R.G. 1971. Flowing Gas-Solids Suspensions. London: Chapman and Hall, Ltd.

12 Streeter, V.L. 1962. Fluid Mechanics, Third Edition, New York: McGraw-Hill Book Co.

13 Schlichting, H. 1968. Boundary Layer Theory, Sixth Edition, New York: McGraw Hill Book Co.

14 Monin, A.S. and Yaglom, A.M. 1971. Statistical Fluid Mechanics: Mechanics of Turbulence. Cambridge: MIT Press.

15 Laufer, J. 1954. The structure of turbulence in fully developed pipe flow. NASA Tech. Rept. 1174.

16 Townes, H.W., Gow, J.L., Powe, R.E., and Weber, N. 1971. Turbulent flow in smooth and rough pipes. ASME Paper 71-WA/FE-7.

17 Wachtell, G.P. and Waggener, J.P. 1964. Flow stability of gas-solids suspensions. The Franklin Institute Report F-B1938.

18 Boothroyd, R.G. 1966. Pressure drop in duct flow of gaseous suspensions of fine particles. Trans. Instn. Chem. Engrs., 44, T306-T313.

19 Boyce, M.P. and Blick, E.F. 1970. Fluid flow phenomena in dusty air. Trans. ASME, J. Basic Engrg., 92, 495-502.

20 Soo, S.L., Trezek, G.J., Dimick, R.C., and Hohnstreiter, G.F. 1964. Concentrations and mass flow distributions in a gas-solid suspension. Ind. Eng. Chem. Fundamentals, 2, 98-106.

21 Kramer, T.J. and Depew, C.A. 1972. Experimentally determined mean flow characteristics of gas-solid suspensions. ASME Paper 72-FE-29.

22 Savins, J.G. and Virk, P.S. (coeditors) 1971. Drag Reduction. Chemical Engineering Progress Symposium Series Volume 67. New York: American Institute of Chemical Engineers.

23 Boothroyd, R.G. 1967. Turbulence characteristics of the gaseous phase in duct flow of a suspension of fine particles. Trans. Instn. Chem. Engrs, 45, T297-T310.

24 Peskin, R.L. and Rin, C.H. 1964. A study of the effect of the presence of suspended solids on LaGrangian properties of fluid turbulence. Technical Report No. 102-ME-F, Dept. of Mech. Engng., Rutgers University.

25 Peskin, R.L. and Wallace, J.P. 1966. Some statistical turbulence properties of the fluid phase in a gas-solid suspension. Technical Report No. 112-ME-F, Dept. of Mech. Engng., Rutgers University.

26 Rodriguez, J.M., Patterson, G.K., and Zakin, J.L. 1969. Turbulence measurements in drag reducing flow. Report from University of Missouri-Rolla.

27 Davies, J.T. 1972. Turbulence Phenomena An Introduction to the Eddy Transfer of Momentum, Mass and Heat, Particularly at Interfaces. New York: Academic Press.

28 Soo, S.L. and Tung, S.K. 1971. Pipe flow of suspensions in turbulent fluid. Electrostatic and gravity effects. Appl. Sci. Res., 24, 83-97.

29 Doig, I.D. and Roper, G.H. 1967. Air velocity profiles in the presence of concurrently transported particles. Ind. Eng. Chem. Fundamentals, 6, 247-256.

30 Reddy, K.V.S., Van Wijk, M.C., and Pei, D.C.T. 1967. Stereophotogrammetry in particle-flow investigations. Report from Dept. of Chem. Engng., University of Waterloo, Ontario.

31 Reddy, K.V.S. and Pei, D.C.T. 1969. Particle dynamics in solids-gas flow in a vertical pipe. Ind. Eng. Chem. Fundamentals, 8, 400-497.

32 Kramer, T.J. and Depew, C.A. 1972. Analysis of mean flow characteristics of gas-solids suspensions. ASME Paper 72-FE-30.

33 Townsend, A.A. 1956. The Structure of Turbulent Shear Flow. Cambridge University Press, Cambridge.

34 Bakewell, H.P. and Lumley, J.L. 1967. Viscous sublayer and adjacent wall region in turbulent pipe flow. Physics of Fluids, 10, 1880-1889.

35 Segler, G. 1951. Pneumatic Grain Conveying. (Silsoe, Beds.: National Institute of Agricultural Engineering).

36 Clark, R.H., Charles, D.E., Richardson, J.F., and Newitt, D.M. 1952. Pneumatic conveying. Part I: The pressure drop during horizontal conveyance. Trans. Instn. Chem. Engrs., 30, 209-224.

37 Halstrom, E.A.N. 1953. Design of experimental apparatus for the study of two-phase flow in circular straight pipe. M.S. Thesis, Princeton U., Princeton, N.J.

38 Depew, C.A. 1960. Heat transfer to flowing gas-solids mixtures in a vertical circular duct. UCRL 9280, Lawrence Radiation Laboratory, U. of Cal., Berkeley, Calif., July 11, 1960.

39 Schluderberg, D.C., Whitelaw, R.L., and Carlson, R.W. 1961. Gaseous suspensions - a new reactor coolant. Nucleonics, 8, 67-73.

40 Hawes, R.E., Holland, E., Kirby, G.T., and Waller, R. 1964. An experimental investigation into heat transfer and pressure drop properties of gaseous suspensions of solids. Atomic Energy Est. Report AEEW-R244.

41 Soo, S.L. and Trezek, G.J. 1966. Turbulent pipe flow of magnesia particles in air. Ind. Eng. Chem. Fundamentals, 5, 388-392.

42 Mason, J.S. and Boothroyd, R.G. 1971. Comparison of friction factors in pneumatically conveyed suspensions using different-sized particles in pipes of varying size. Paper C1, Proc. 1st Int. Conf. on Pneumatic Transport of Solids in Pipes, BHRA Fluid Engng., Cranfield, U.K. (September 1971).

43 Peters, L.K., Bender, D.W., and Klinzing, G.E. 1972. Friction modification in a coupled system. Paper 20f, AIChE Annual Meeting.

Table 1

Experimental Evidence of Drag Reduction

Reference	Solids Diameter and Type	Pipe Diameter and Orientation	Loading Ratio	Reynolds Number
Segler 1951 (ref. 35)	wheat grains	9" horizontal	0-30.0	200,000-250,000
Clark et.al. 1952 (ref.36)	1060μ cress	1" horizontal	1.5-5	12,000-68,000
Halstrom 1953 (ref. 37)	200μ glass	-----	---	----
Depew 1960 (ref. 38)	30μ glass	0.71" vertical	0-5.0	13,500
			0-3.5	27,400
Richardson et.al. 1960 (ref. 6)	1460μ perspex	1" horizontal	0-1.0	12,000-70,000
Schluderberg et.al. 1961 (ref. 39)	1-5μ graphite	0.532" vertical	0-12.0	20,000-200,000
Sproull 1961 (ref. 4)	-----	----	0.21	----
Hawes et.al. 1964 (ref. 40)	0-5μ graphite	0.5" vertical	---	----
Boothroyd 1966 (ref. 18)	0-40μ zinc	1" vertical	0-3.0	35,000
			0-7.0	53,000
			0-12.0	80,000
			0-12.0	100,000
		2" vertical	0-2.0	35,000
			0-2.5	53,000
			0-2.5	80,000
			0-2.5	100,000
		3" vertical	0-1.0	53,000
			0-1.5	80,000
Soo et.al. 1966 (ref. 41)	30μ magnesia	5" horizontal	0-1.0	130,000-295,000

Table 1 (cont.)

Experimental Evidence of Drag Reduction

Reference	Solids Diameter and Type	Pipe Diameter and Orientation	Loading Ratio	Reynolds Number
Boyce et.al. 1970 (ref. 19)	2-60μ silica	2.75" angulated	0-3.5	18,200-63,000
	100μ glass		0-4.0	9,450-63,000
	200μ glass		0-4.0	12,000-63,000
	840μ glass		0-5.0	40,400-63,000
	1680μ glass		0-6.0	13,800-63,000
Mason et.al. 1971 (ref. 42)	15,40,70μ alumina	1" vertical	0-6.0	140,000
			0-4.0	75,000
	15μ alumina		0-1.0	57,000
	15,40μ alumina	2" vertical	0-1.0	70,000
	15μ alumina		0-1.0	85,500
			0-1.0	105,000
	15,40,70μ alumina	3" vertical	0-1.5	69,500
Peters et.al. 1972 (ref. 43)	25μ glass	1" vertical	0.8-1.4	15,000-25,000
Rossetti et.al. 1972 (ref. 2)	10μ glass	1" vertical	0-1.5	24,250
	20μ glass		0-0.4	13,150
			0-0.7	16,700
			0-2.0	22,750
	25μ glass		0-0.4	13,000
			0-0.6	16,250
			0-1.8	22,800
	34μ glass		0-0.7	12,000
			0-0.9	15,450
			0-1.5	22,300
	59μ glass		0-0.6	12,500
			0-0.7	16,400
			0-1.0	21,800
	10μ glass	0.870" horizontal	0-1.5	27,700
	20μ glass		0-0.4	15,000
			0-0.6	19,100

Table 1 (cont.)

Experimental Evidence of Drag Reduction

Reference	Solids Diameter and Type	Pipe Diameter and Orientation	Loading Ratio	Reynolds Number
Rossetti et.al. 1972 (ref. 2) (cont.)	20μ glass	0.870"horizontal	0-2.0	25,925
	25μ glass		0-1.0	18,800
			0-2.5	25,900

Table 2

Average Particle Diameters

Bead Designation	Weight Mean Diameter Before, After Circulation (microns)	Arithmetic Mean Diameter Before, After Circulation (microns)
#980	15.0, 13.1	11.0, 11.5
#981	21.0, 20.2	17.4, 14.4
#279	21.6, 22.4	16.7, 15.0
#380	36.0, 35.0	28.0, 17.6
#660	55.0, 18.0	34.0, 9.4

Figure 1

Closed Loop System

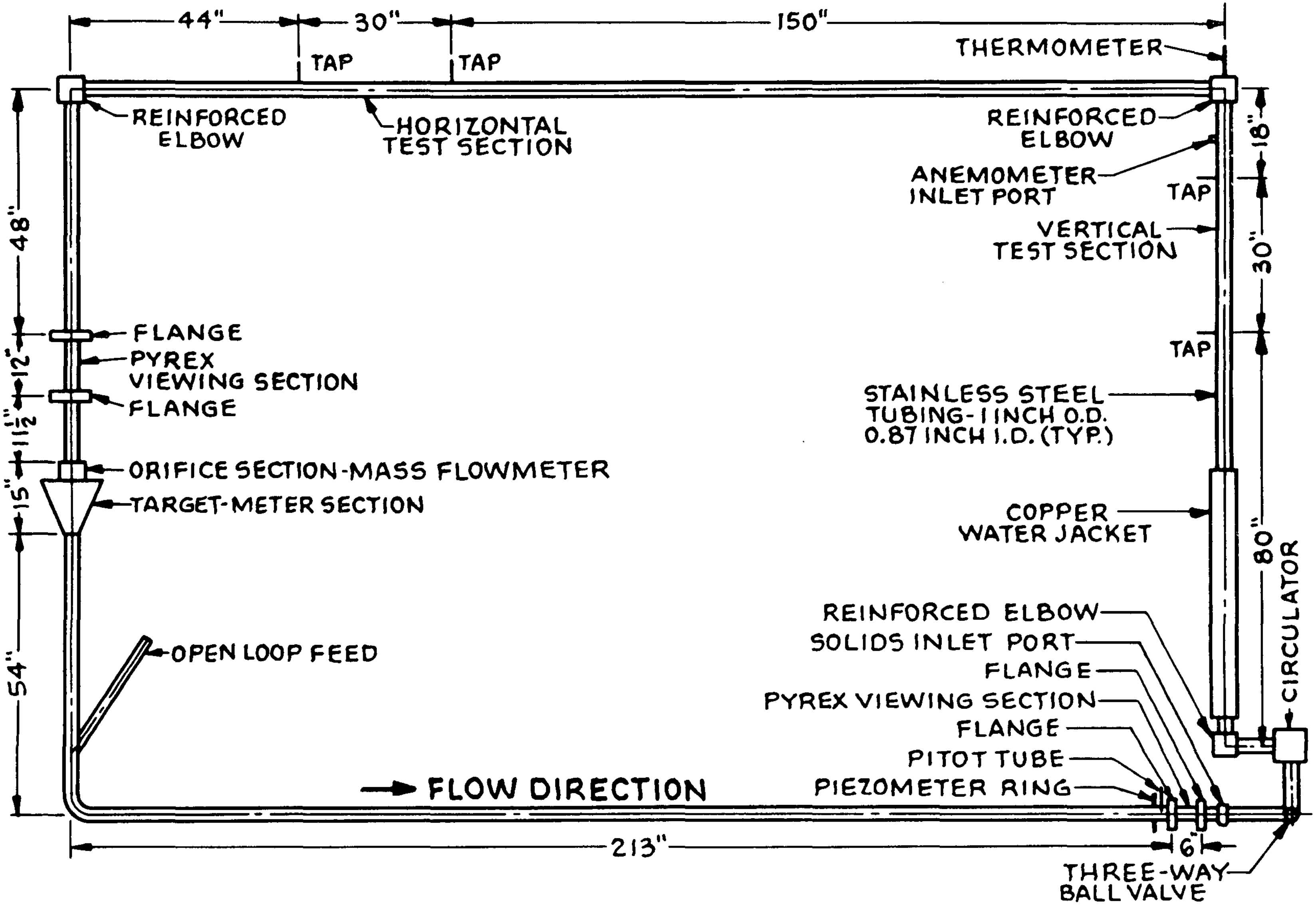

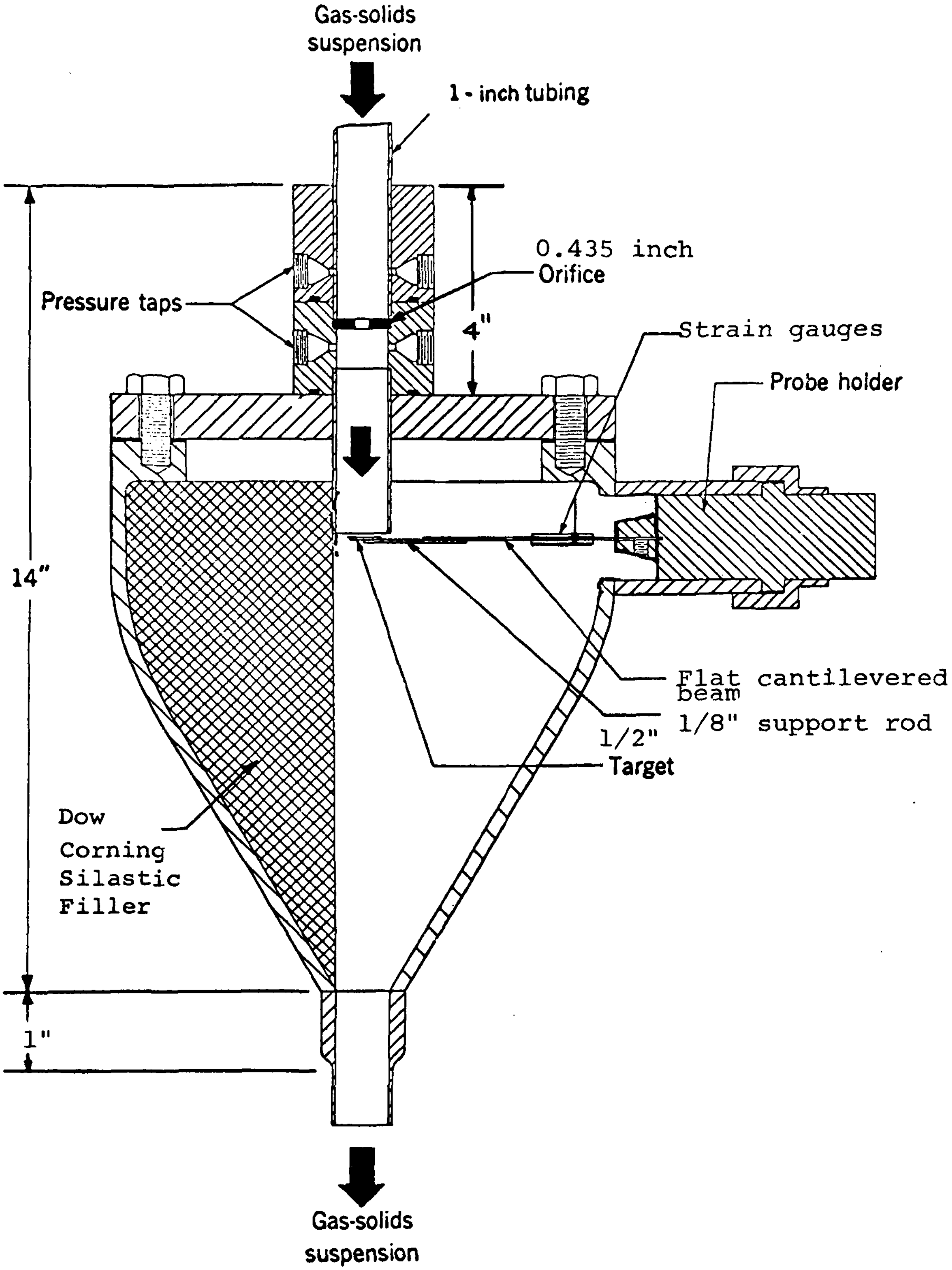

Figure 2

Mass Flowmeter

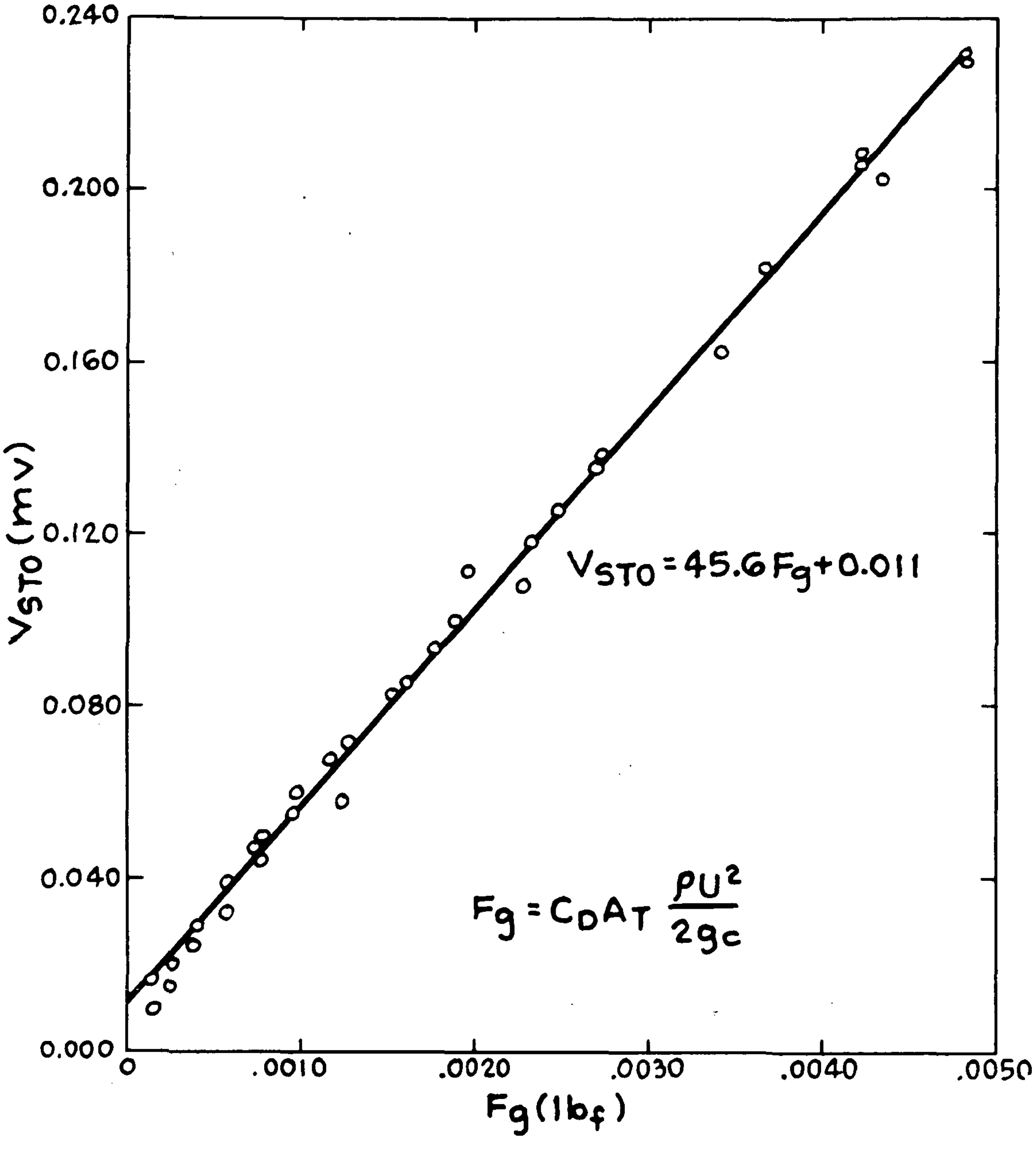

Figure 3

Recorder Output Voltage Versus Air Drag Force

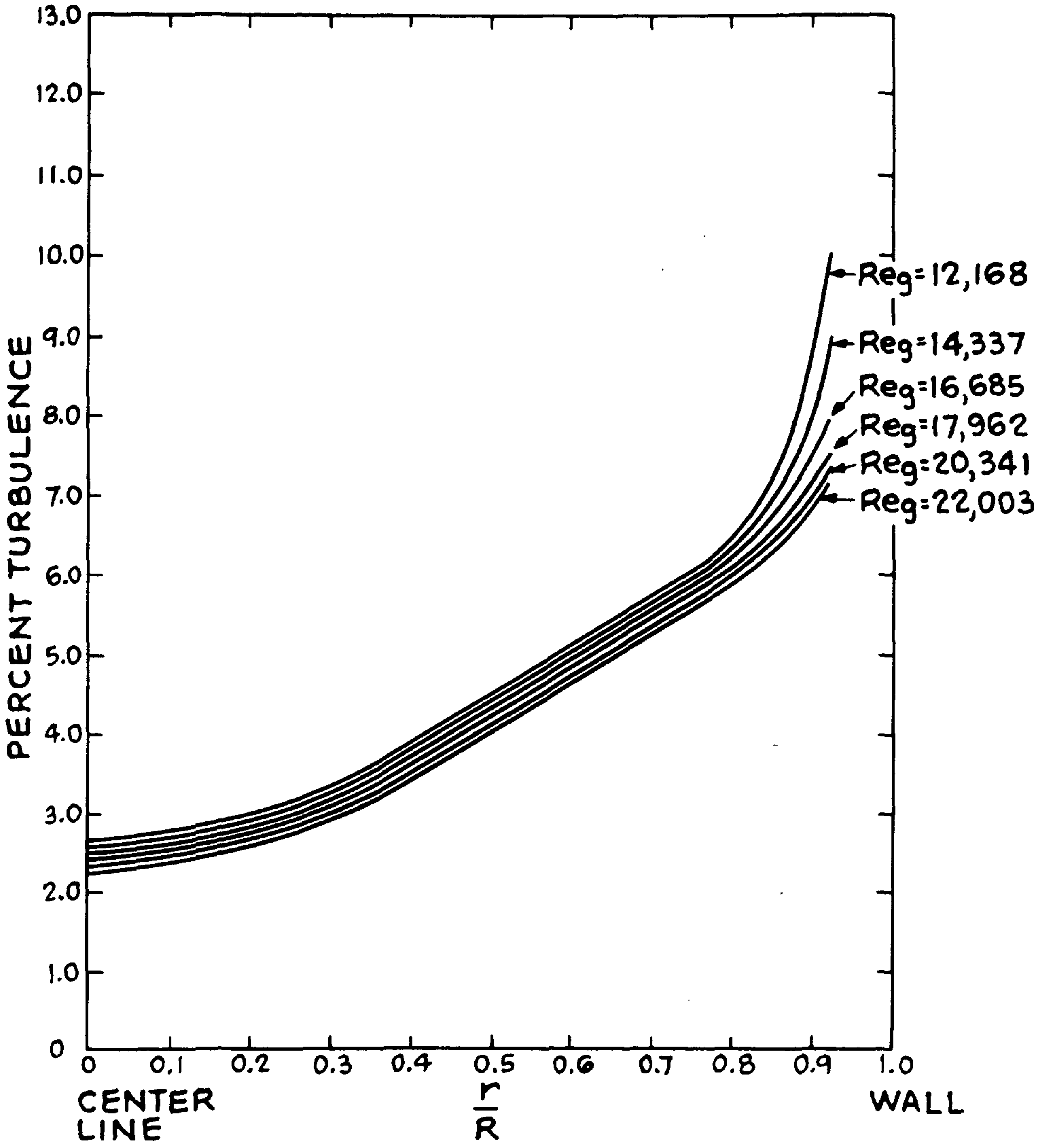

Figure 4

Clean Air Turbulence Intensities - Fiber-Film Measurements

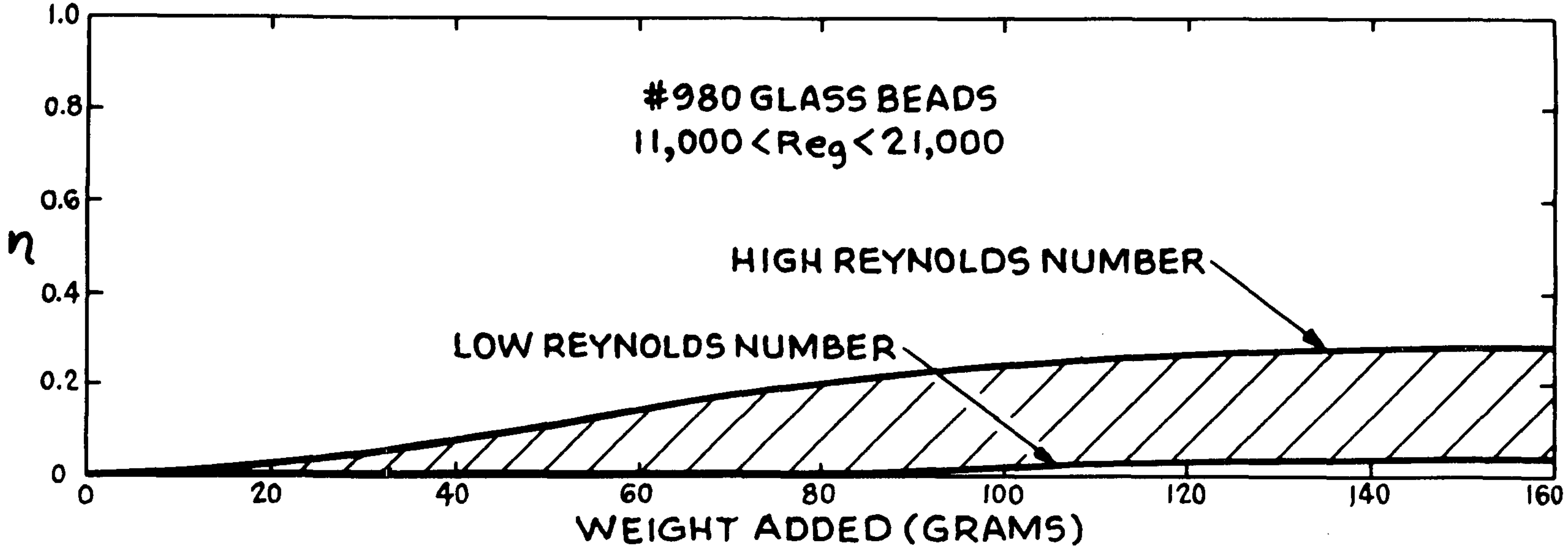

Figure 5

Loading Ratio Versus Weight Added - #980 Glass Beads

Figure 6

Loading Ratio Versus Weight Added - #380 Glass Beads

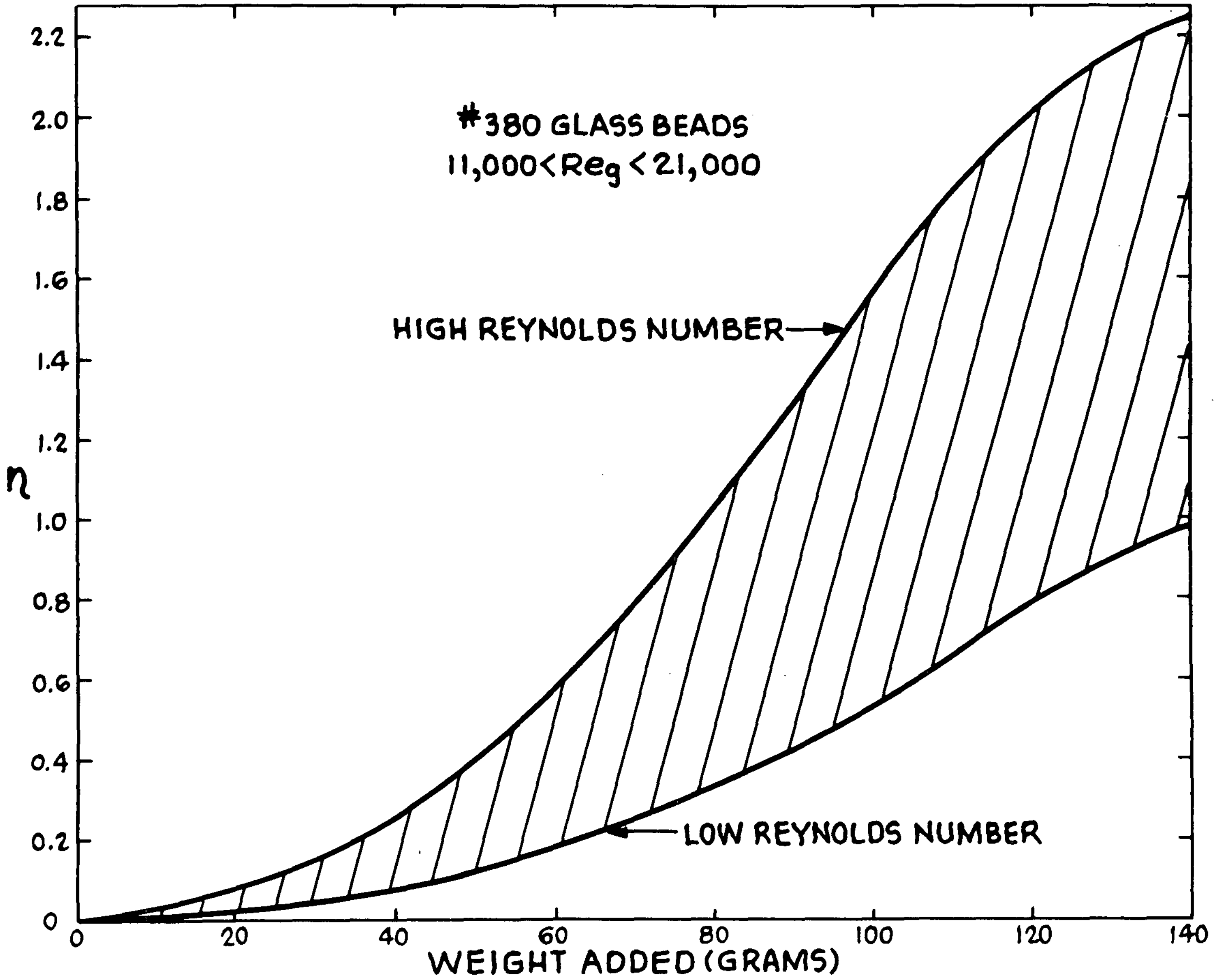

Figure 7 Vertical Friction Factor Ratio Versus Loading Ratio - #980, #981, and #279 Glass Beads

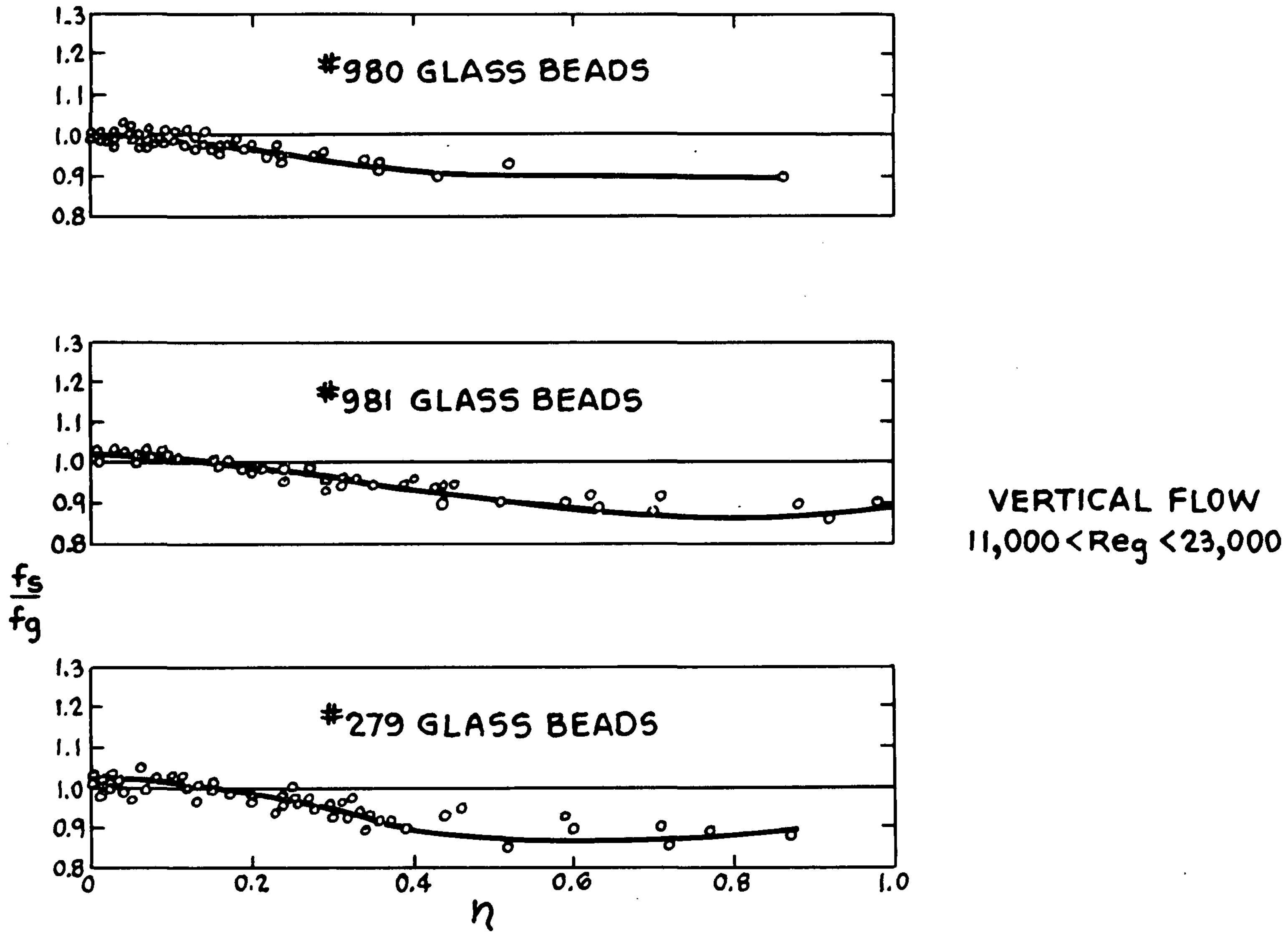

Figure 8 Vertical Friction Factor Ratio Versus Loading Ratio - #380 Glass Beads

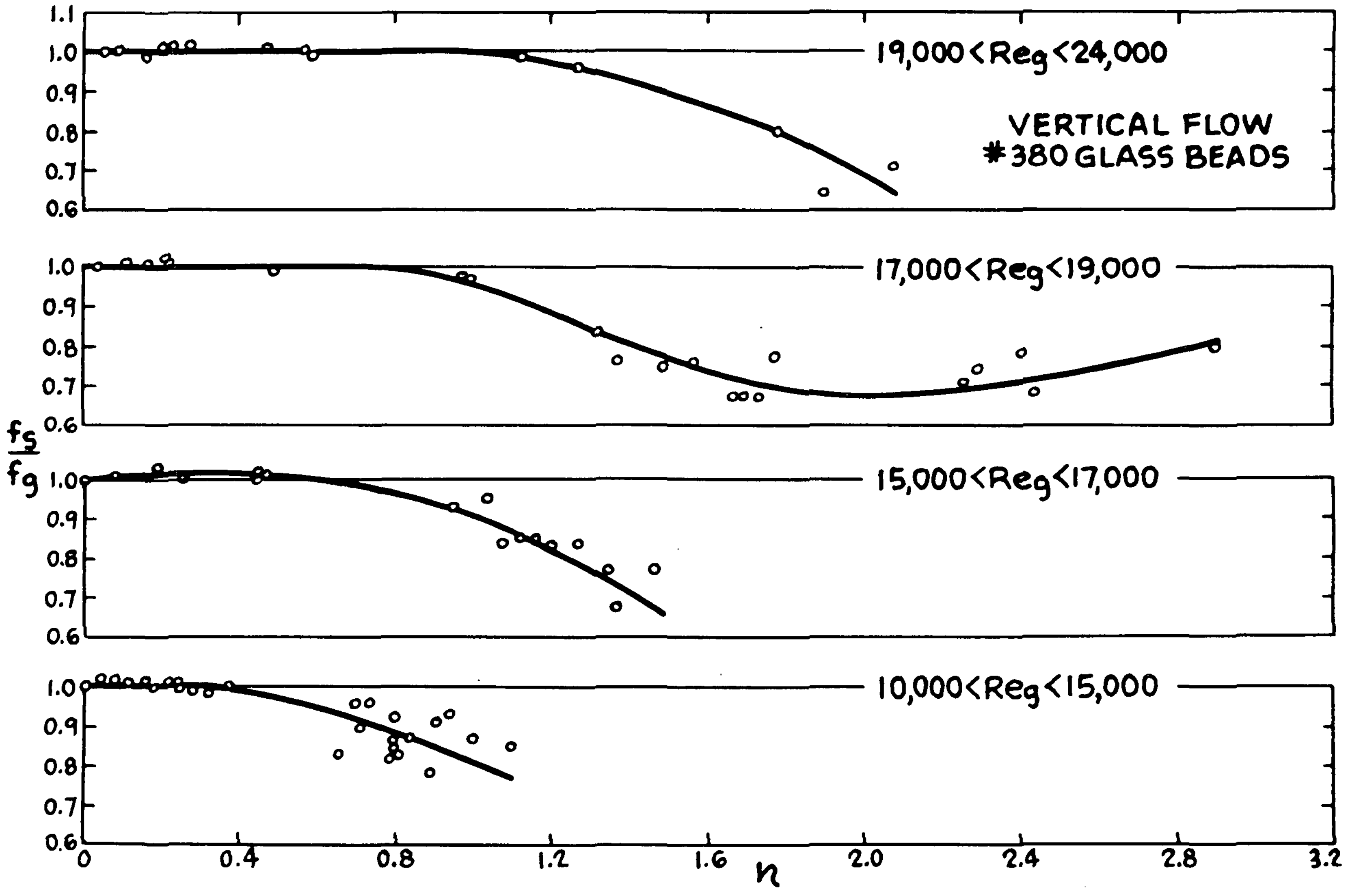

Figure 9 Vertical Friction Factor Ratio Versus Loading Ratio - #660 Glass Beads

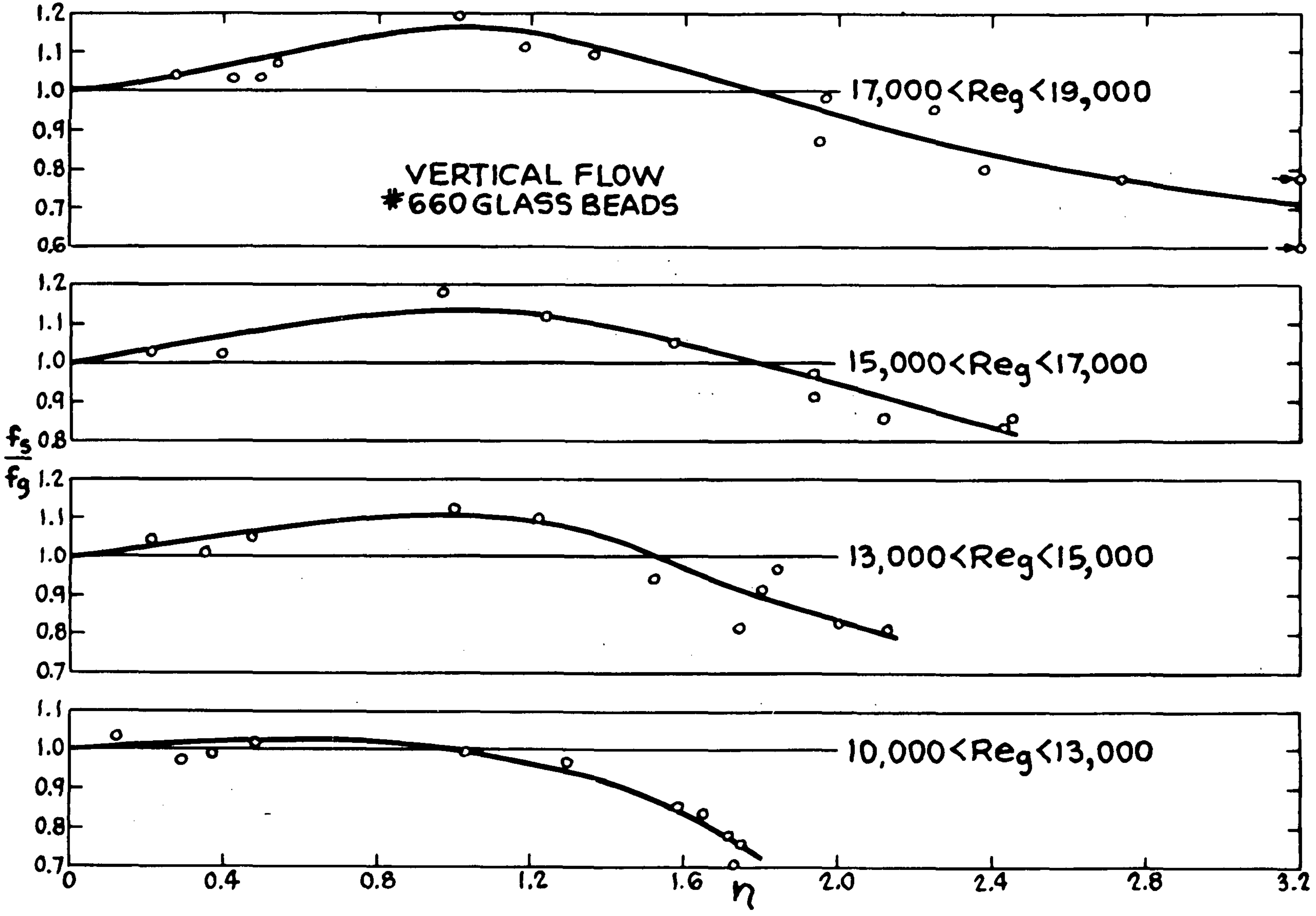

Figure 10 Horizontal Friction Factor Ratio Versus Loading Ratio - #980, #981, and #279 Glass Beads

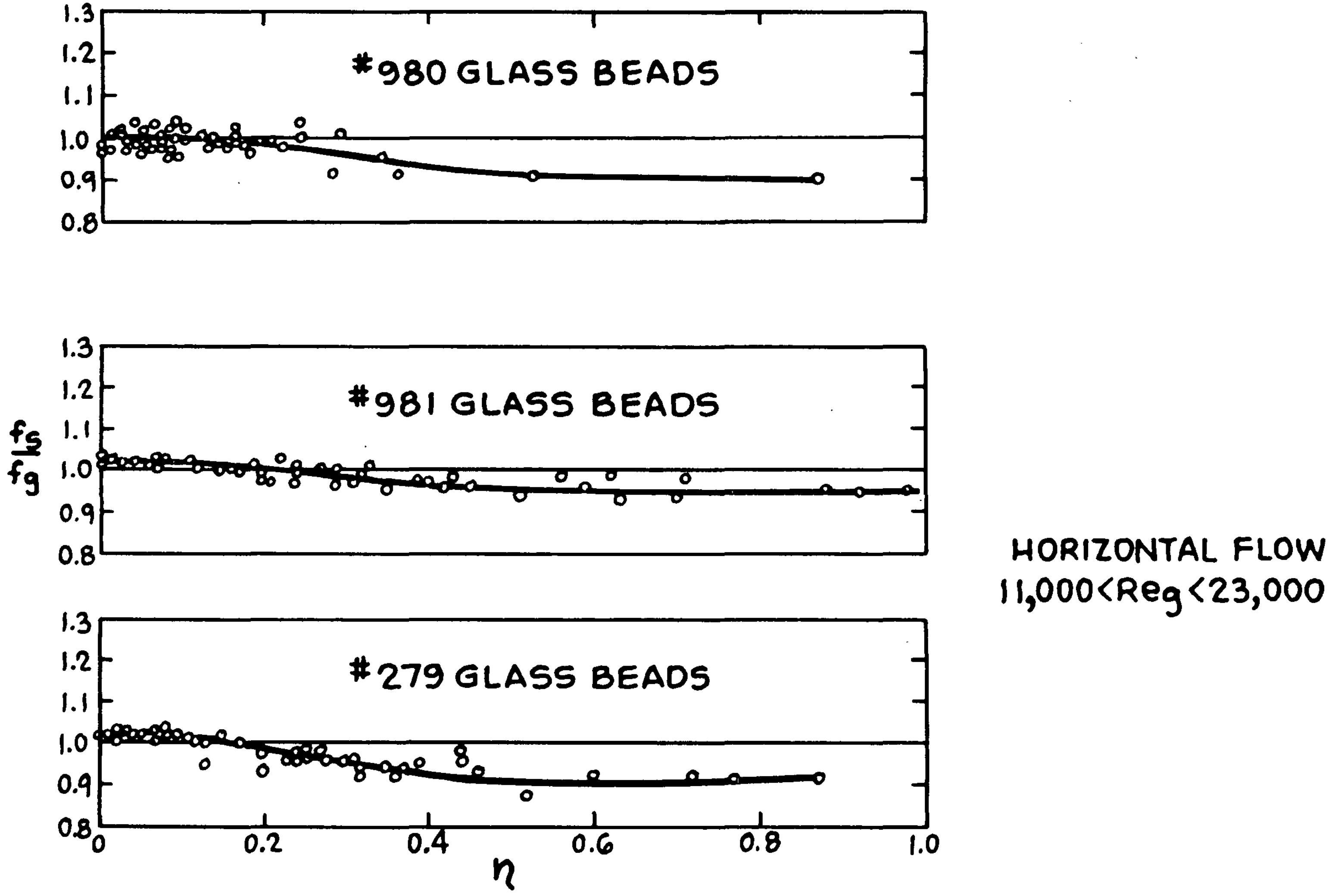

Figure 11 Horizontal Friction Factor Ratio Versus Loading Ratio - #380 and #660 Glass Beads

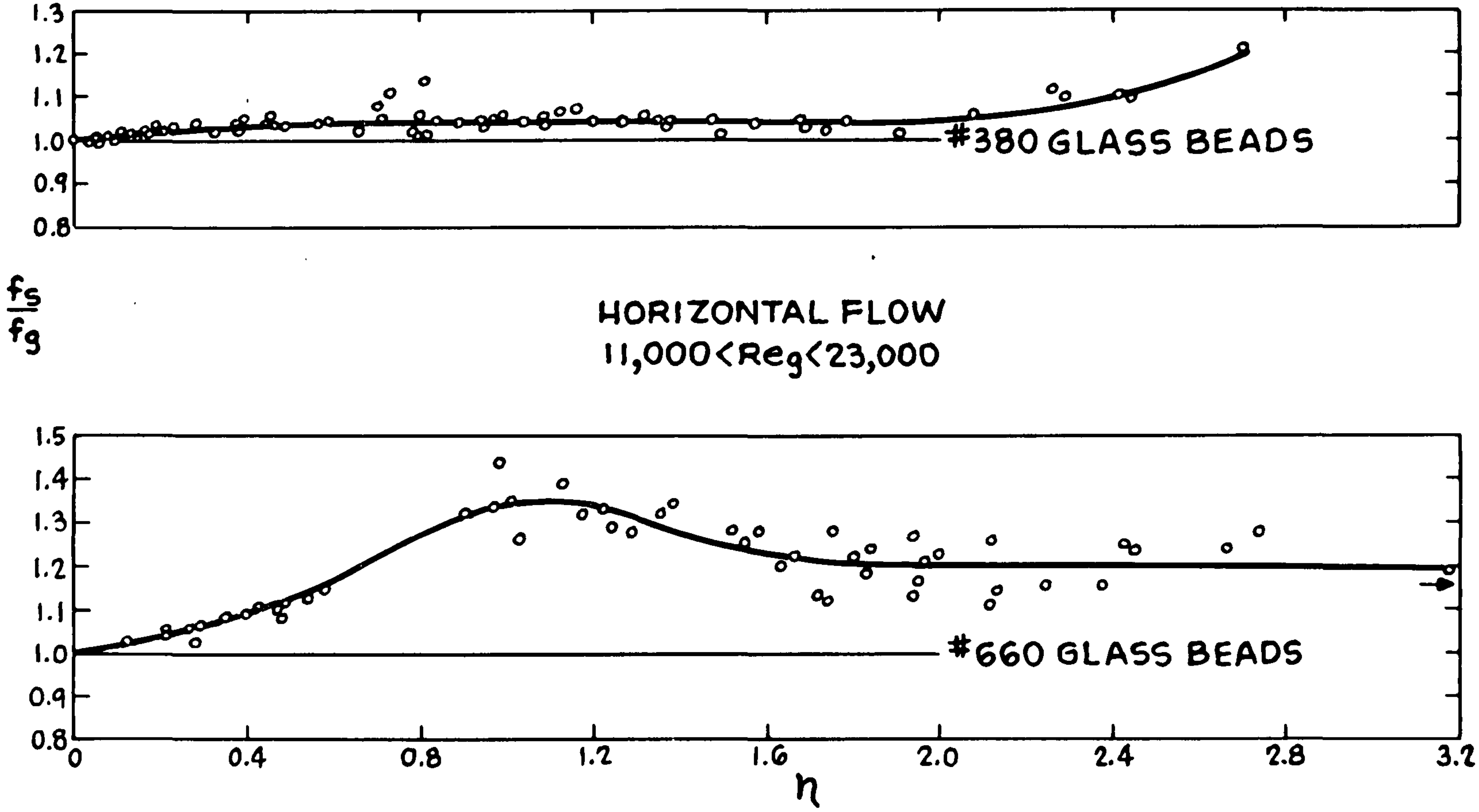

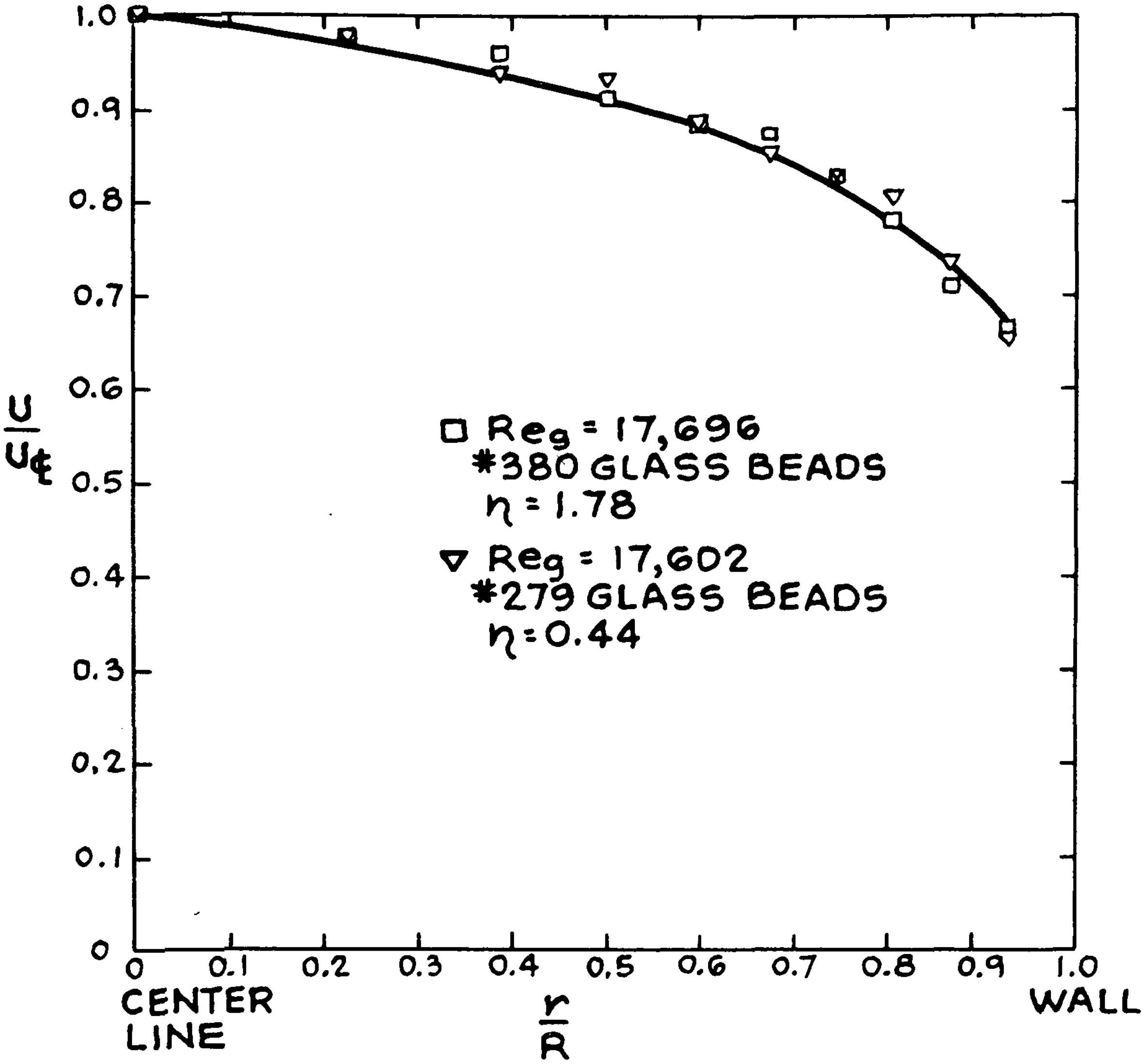

Figure 12

Suspension Air Velocity Profiles

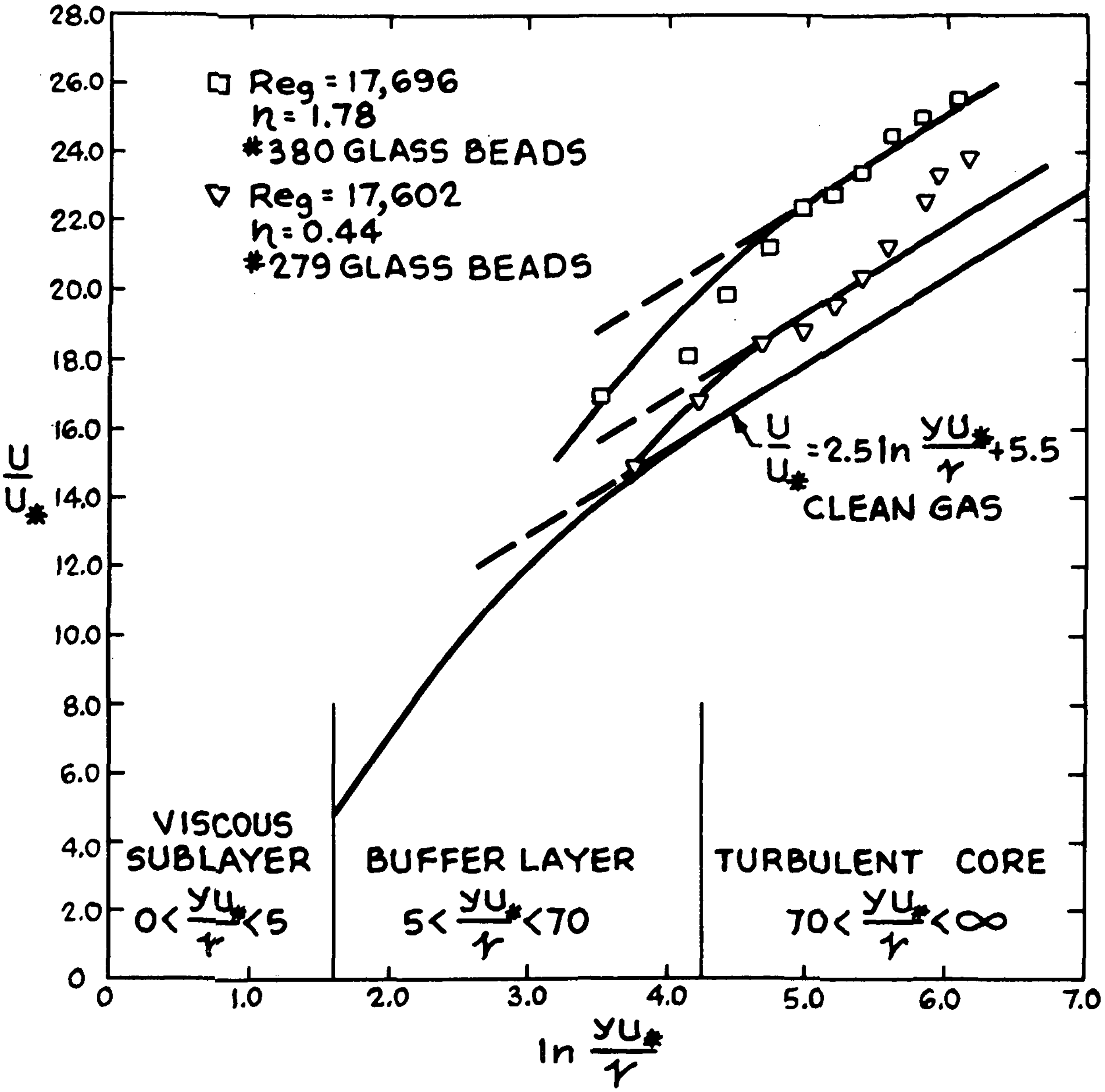

Figure 13 Suspension Air Velocity Profiles and the Universal Velocity Profile

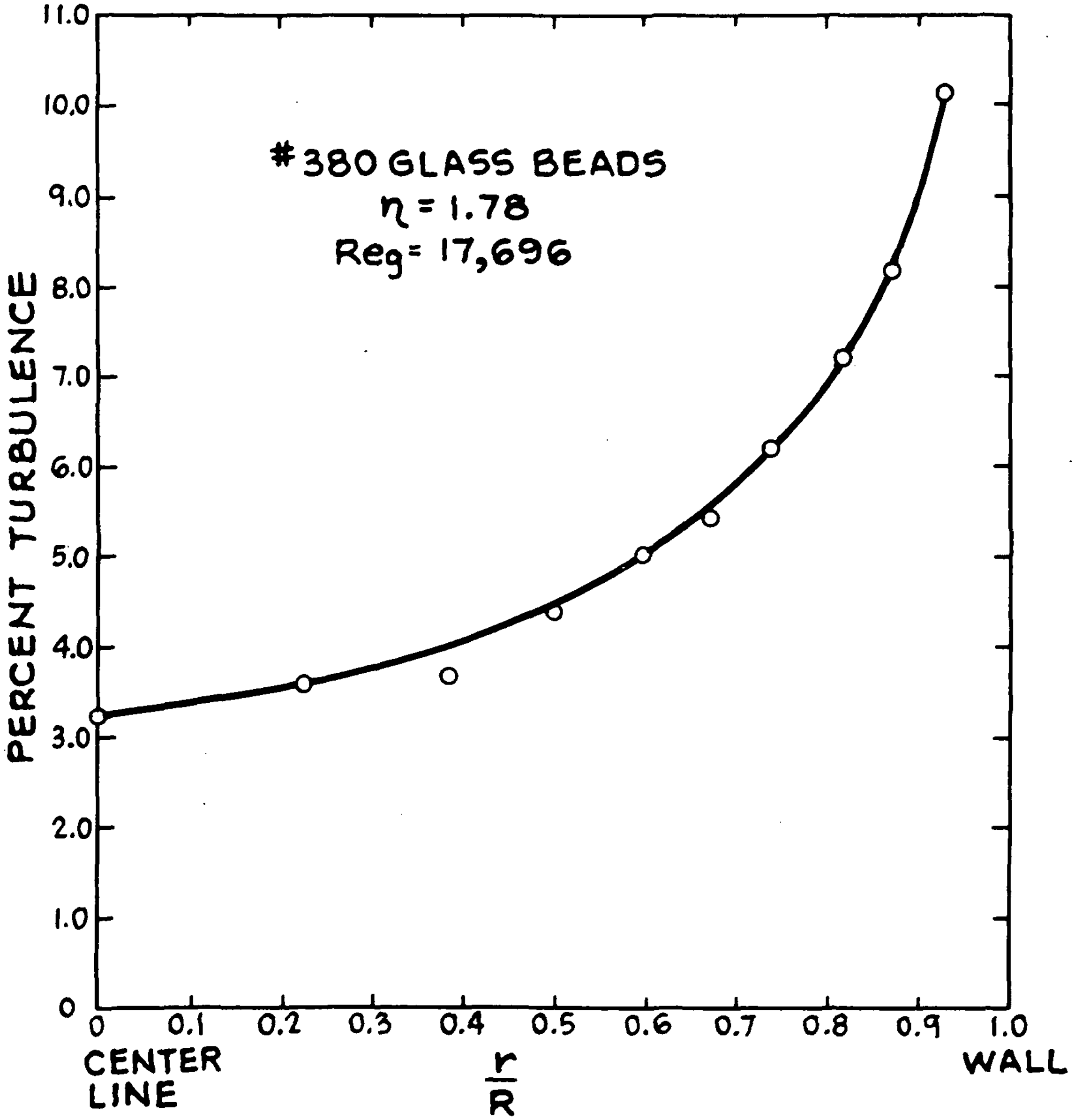

Figure 14 Suspension Air Turbulence Intensity Profile - #380 Glass Beads

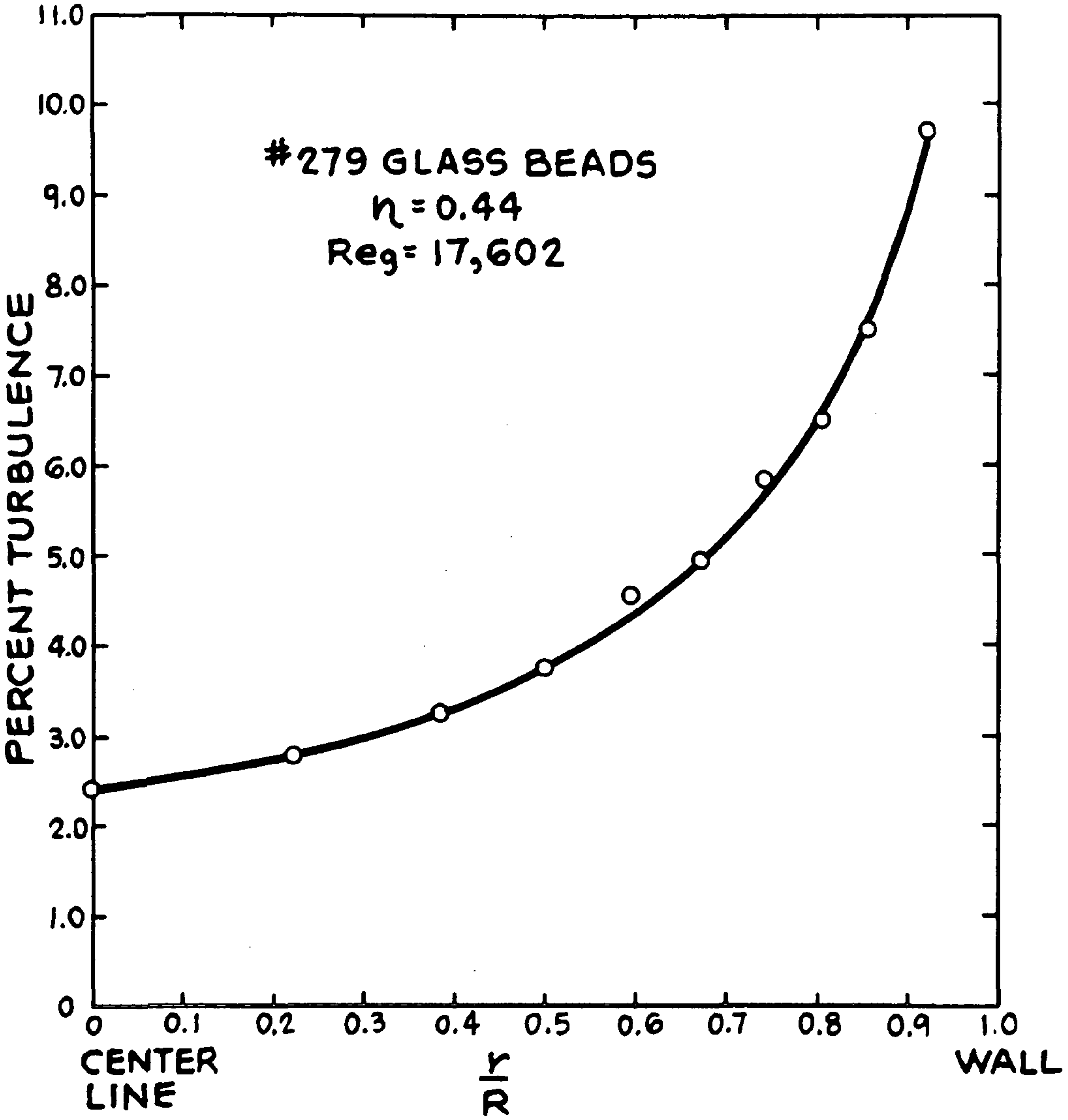

Figure 15 Suspension Air Turbulence Intensity Profile - #279 Glass Beads

Figure 16 Suspension Air Turbulence Intensities Normalized with Friction Velocity

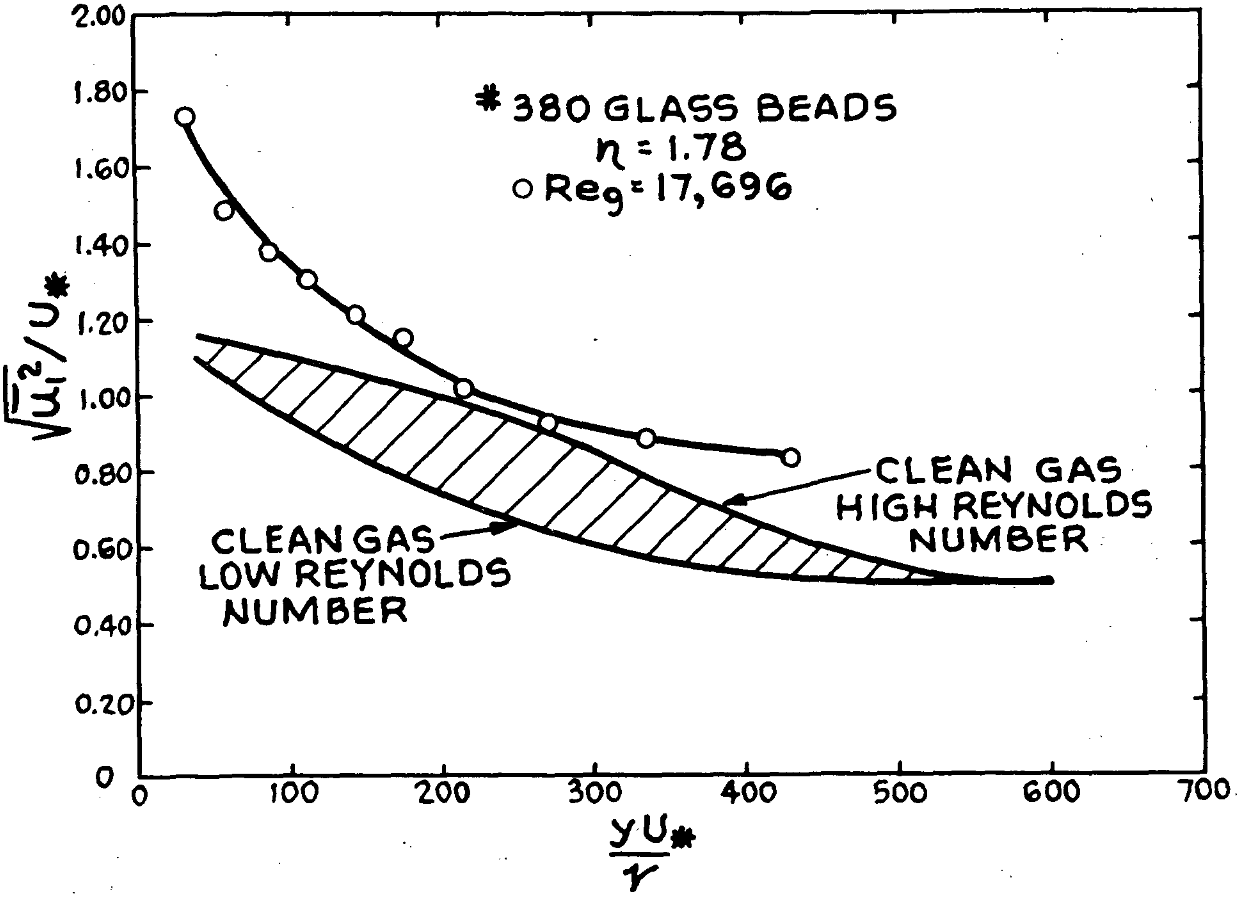

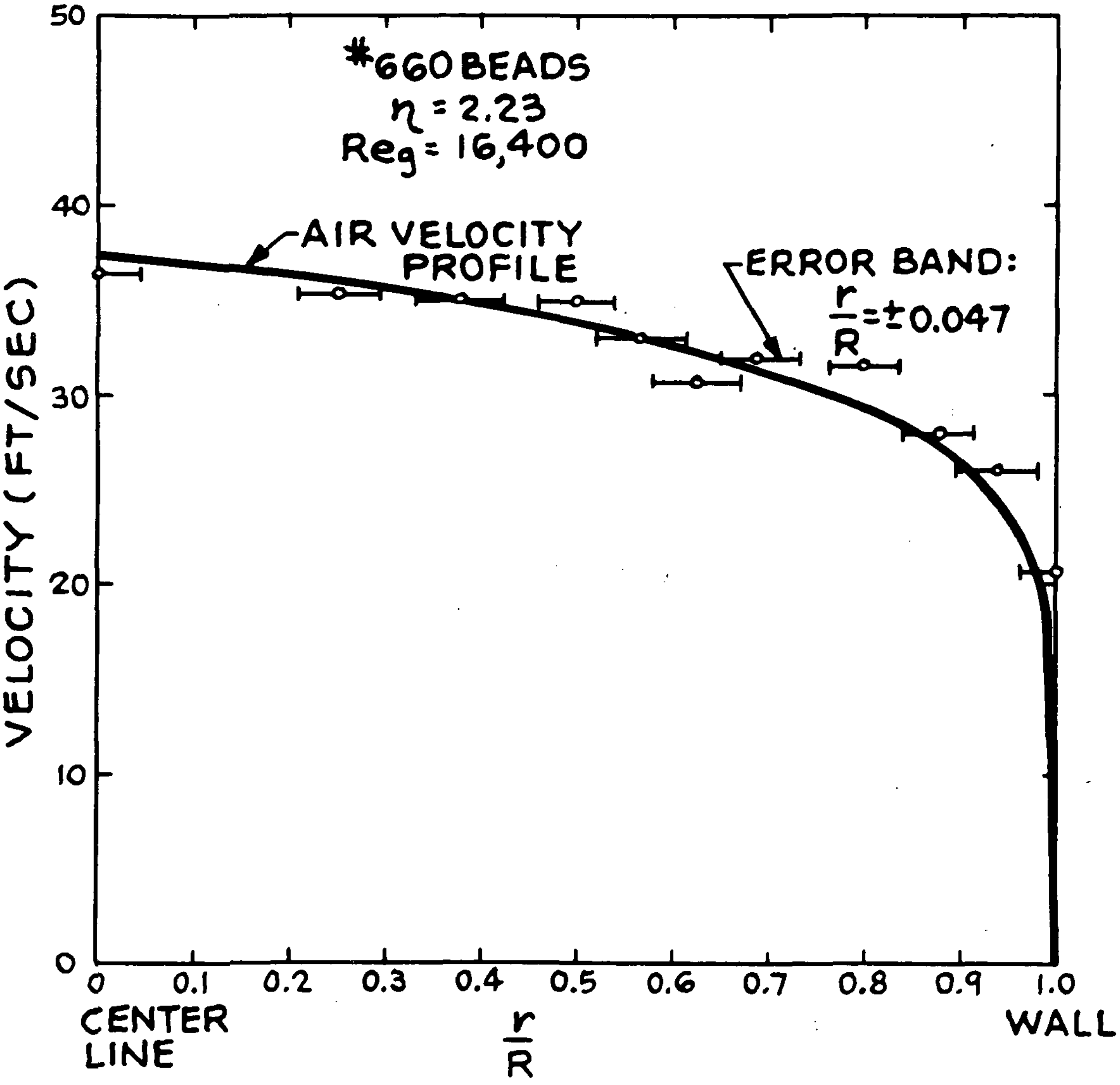

Figure 17

Particle Velocity Profile

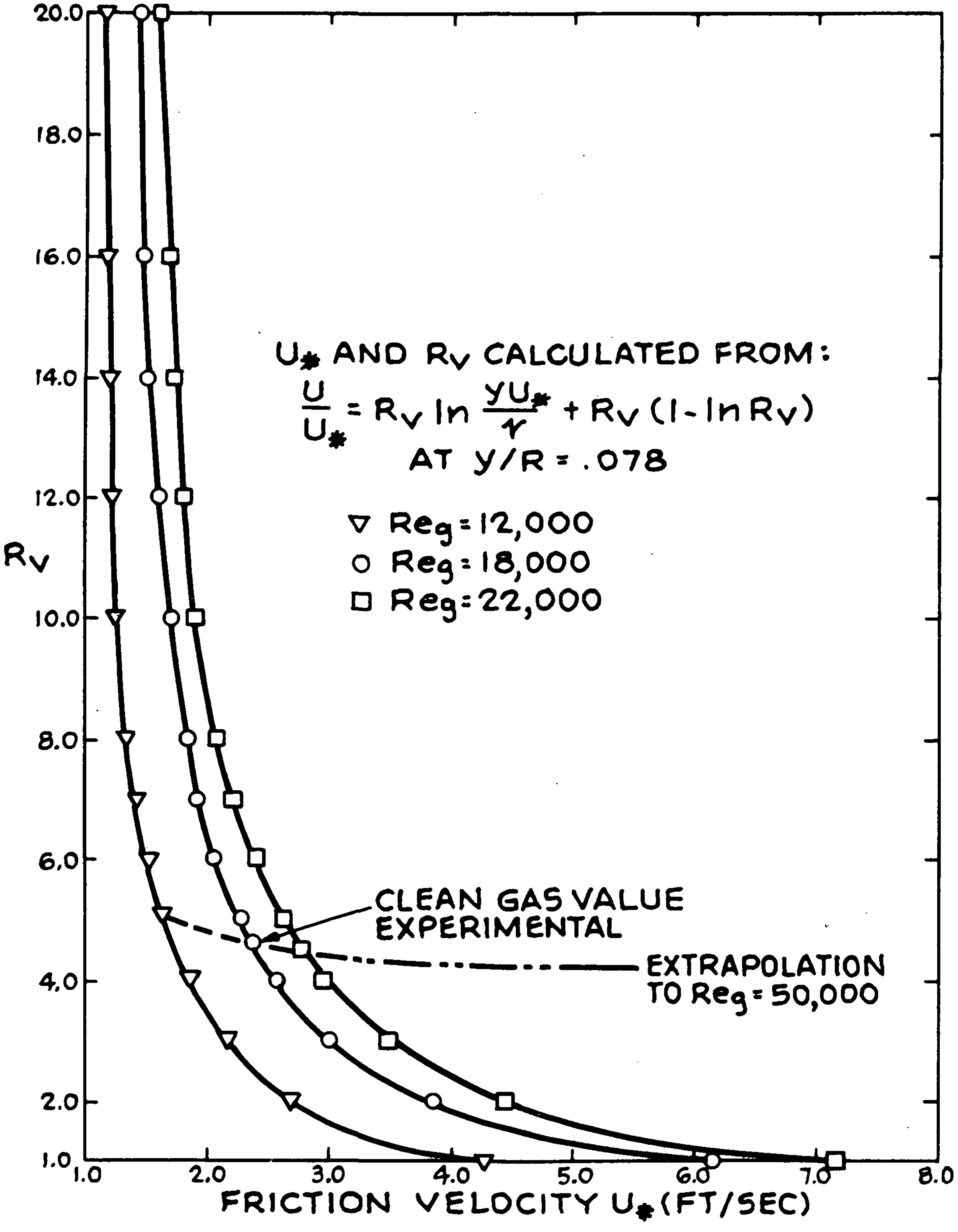

Figure 18 Dimensionless Sublayer Thickness as a Function of Friction Velocity

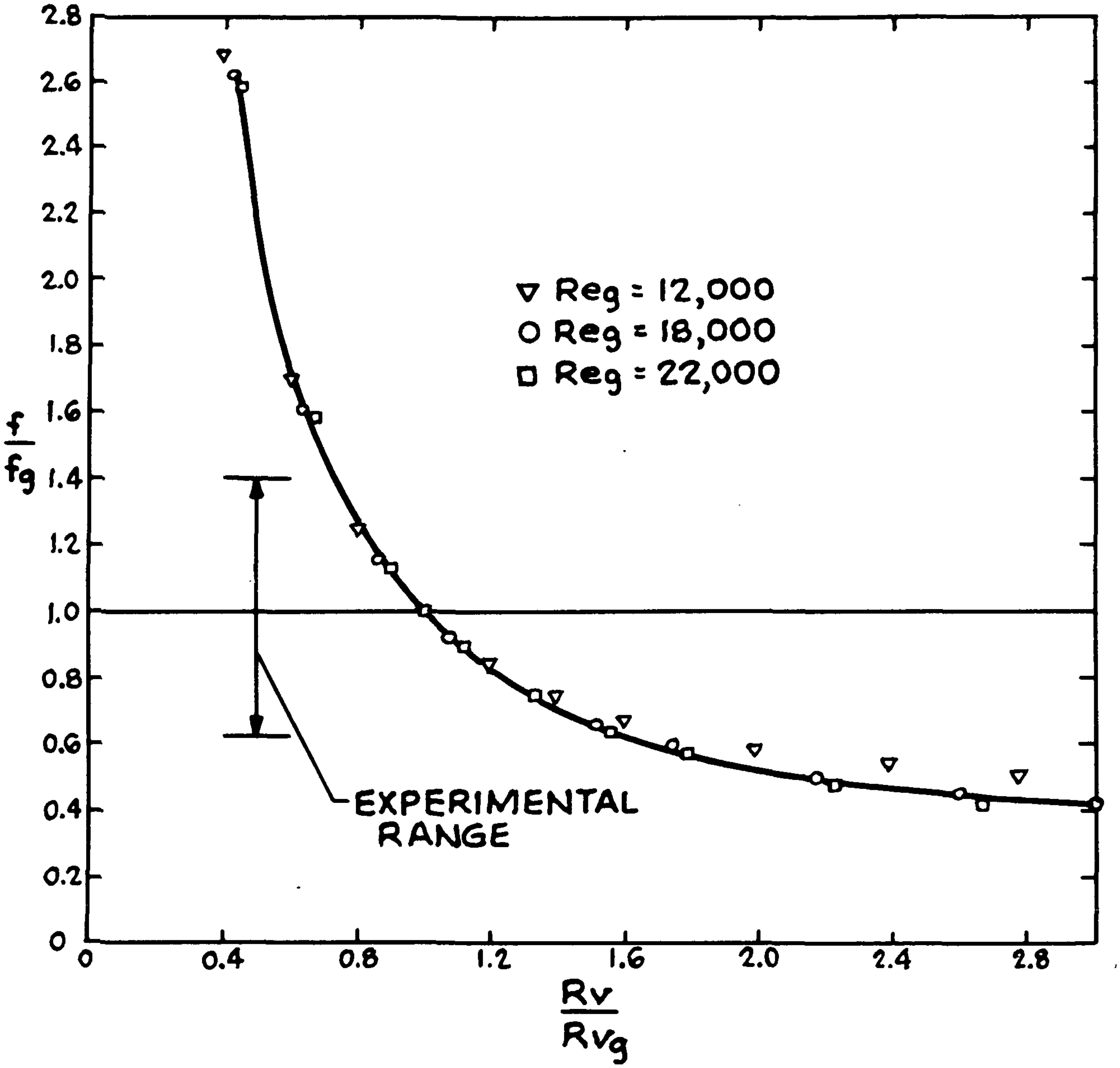

Figure 19 Friction Factor Ratio Versus Dimensionless Sublayer Thickness Ratio

Figure 20 Friction Factor Ratio Versus Loading Ratio Based Upon Modified Analysis with Variable Production

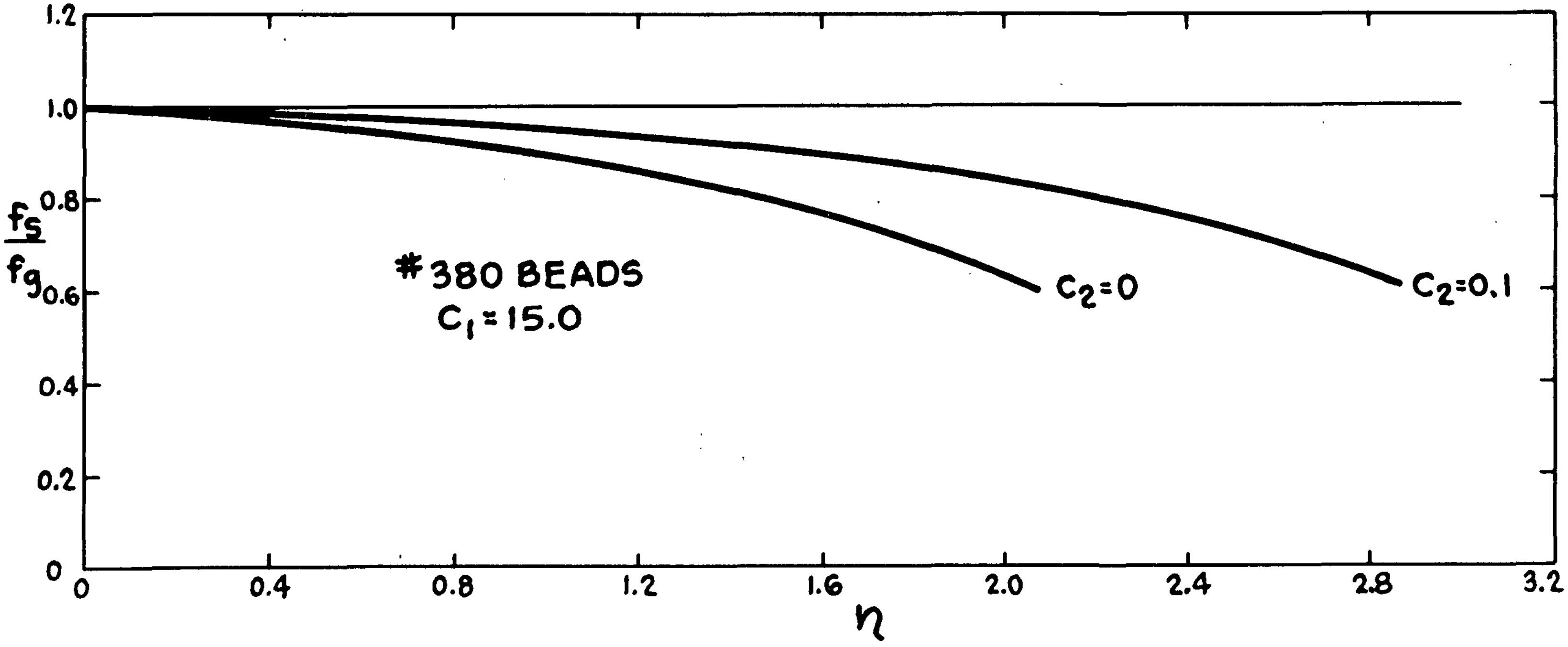

Figure 21 Friction Factor Ratio Versus Loading Ratio Based Upon Modified Analysis with Variable Particle Size

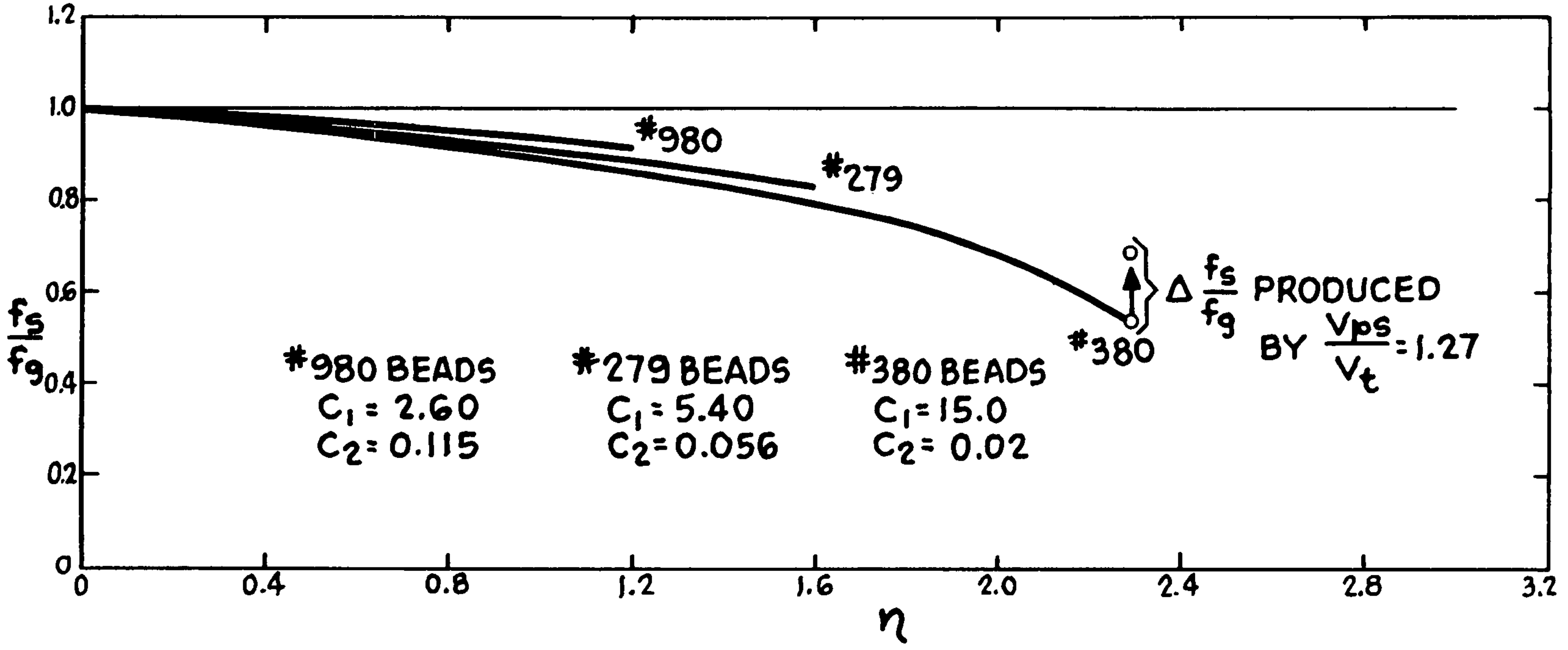

NASA-Langley, 1973 —— 12 E-7410

NATIONAL AERONAUTICS AND SPACE ADMINISTRATION
WASHINGTON, D.C. 20546

OFFICIAL BUSINESS
PENALTY FOR PRIVATE USE $300

SPECIAL FOURTH-CLASS RATE
BOOK

POSTAGE AND FEES PAID
NATIONAL AERONAUTICS AND
SPACE ADMINISTRATION
451

U.S.MAIL

POSTMASTER: If Undeliverable (Section 158 Postal Manual) Do Not Return

"The aeronautical and space activities of the United States shall be conducted so as to contribute . . . to the expansion of human knowledge of phenomena in the atmosphere and space. The Administration shall provide for the widest practicable and appropriate dissemination of information concerning its activities and the results thereof."

—NATIONAL AERONAUTICS AND SPACE ACT OF 1958

NASA SCIENTIFIC AND TECHNICAL PUBLICATIONS

TECHNICAL REPORTS: Scientific and technical information considered important, complete, and a lasting contribution to existing knowledge.

TECHNICAL NOTES: Information less broad in scope but nevertheless of importance as a contribution to existing knowledge.

TECHNICAL MEMORANDUMS: Information receiving limited distribution because of preliminary data, security classification, or other reasons. Also includes conference proceedings with either limited or unlimited distribution.

CONTRACTOR REPORTS: Scientific and technical information generated under a NASA contract or grant and considered an important contribution to existing knowledge.

TECHNICAL TRANSLATIONS: Information published in a foreign language considered to merit NASA distribution in English.

SPECIAL PUBLICATIONS: Information derived from or of value to NASA activities. Publications include final reports of major projects, monographs, data compilations, handbooks, sourcebooks, and special bibliographies.

TECHNOLOGY UTILIZATION PUBLICATIONS: Information on technology used by NASA that may be of particular interest in commercial and other non-aerospace applications. Publications include Tech Briefs, Technology Utilization Reports and Technology Surveys.

Details on the availability of these publications may be obtained from:

SCIENTIFIC AND TECHNICAL INFORMATION OFFICE

NATIONAL AERONAUTICS AND SPACE ADMINISTRATION

Washington, D.C. 20546